

Numerical Assessment of Morphological and Hydraulic Properties of Moss, Lichen and Peat from a Permafrost Peatland

Simon Cazaurang¹, Manuel Marcoux¹, Oleg S. Pokrovsky^{2,3}, Sergey V. Loiko³, Artem G. Lim³, Stéphane Audry², Liudmila S. Shirokova^{2,4}, Laurent Orgogozo²

¹ Toulouse Institute of Fluid Mechanics (IMFT), National Polytechnic Institute of Toulouse, Toulouse, F-31400, France.

² Geosciences Environnement Toulouse (GET) Laboratory, University Toulouse III – Paul Sabatier, Toulouse, F-31400, France.

³ BIO-GEO-CLIM Laboratory, Tomsk State University, Tomsk, Russian Federation.

⁴ N. Laverov Federal Center for Integrated Arctic Research of the Ural Branch – Russian Academy of Science, Russian Federation.

Correspondence to:

Simon Cazaurang
Institut de Mécanique des Fluides de Toulouse
2, Allée du Professeur Camille Soula
F-31400 Toulouse, France
mail: simon.cazaurang@imft.fr
tel: +33 534-322-956

Abstract. Due to its insulating and draining role, assessing ground vegetation cover properties is important for high resolution hydrological modeling of permafrost regions.. In this study, morphological and effective hydraulic properties of Western Siberian Lowland ground vegetation samples (lichens, *Sphagnum* mosses, peat) are numerically studied based on tomography scans. Porosity is estimated through a void voxels counting algorithm, showing the existence of representative elementary volumes (REV) of porosity for most samples. Then, two methods are used to estimate hydraulic conductivity depending on the sample's homogeneity. For homogeneous samples, Direct Numerical Simulations of a single-phase flow are performed, leading to a definition of hydraulic conductivity related to a REV, which is larger than those obtained for porosity. For heterogeneous samples, no adequate REV may be defined. To bypass this issue, a pore network representation is created from computerized scans. Morphological and hydraulic properties are then estimated through this simplified representation. Both methods converged on similar results for porosity. Some discrepancies are observed for specific surface area. Hydraulic conductivity fluctuates by two orders of magnitude, depending on the method used.

Porosity values are in line with previous values found in the literature, showing that arctic cryptogamic cover can be considered as an open and well-connected porous medium (over 99% of overall porosity is open porosity). Meanwhile, digitally estimated hydraulic conductivity is higher compared to previously obtained results based on field and laboratory experiments. However, the uncertainty is less than in experimental studies available in the literature. Therefore, biological and sampling artefacts are predominant over numerical biases. This could be related to compressibility effects, occurring during field or laboratory measurements. These numerical methods lay a solid foundation for interpreting the homogeneity

35 of any type of sample, and processing some quantitative properties' assessment, either with image processing or with pore network model. The main observed limitation is the input data quality (e.g. the tomographic scans' resolution) and its pre-processing scheme. Thus, some supplementary studies are compulsory for assessing syn-sampling and syn-measurement perturbations in experimentally estimated, effective hydraulic properties of such a biological porous medium.

40 **Table 1 location**

1. Introduction

Covering a quarter of the Northern Hemisphere's land surface (Brown et al., 1997), permafrost soils are the most representative soil types in arctic and subarctic regions. Permafrost is a soil layer in which temperature remains below zero degrees for at least two consecutive years, thus holding ice in its porous structure. Frozen layers make permafrost hydrology peculiar, resulting in complex couplings between heat and water fluxes (Grenier et al., 2018; Tananev et al., 2020). Seasonal structural variations occur in permafrost soils, as surface thawing forms an 'active layer'. Most permafrost-related biogeochemical processes (especially organic matter degradation) take place in this layer. The active layer is at its maximum thickness in the early autumn, and is generally meters in scale (Clayton et al., 2021; Aalto et al., 2018; Guo & Wang, 2017). Active layer thickness is, nonetheless, spatially variable due to climatic conditions, land cover, and the micro and macro-topography. The impact of hydrological climate change is particularly drastic in permafrost-dominated environments because of deepening thaw fronts (Hinzman & Kane, 1992). Indeed, between 2008 and 2016, the average annual temperature of arctic permafrost soil increased by $0.4 (\pm 0.25)^{\circ}\text{C}$ (Biskaborn et al., 2019; Fox-Kemper et al., in press). This causes positive feedback on average atmospheric temperatures (Meredith et al., 2019), reduces latent heat effects (Walwood & Kurylyk, 2016) and increases water drainage in Arctic watersheds (Liljedahl et al., 2016). Hence, quantifying heat and water transfer properties in permafrost affected regions is compulsory.

Previous studies have addressed this quantification through field observations (Olefeldt & Roulet, 2014; Streletskiy et al., 2015; Throckmorton et al., 2016; O'Connor et al., 2020, among others) or field and laboratory experiments (Vedie et al., 2011; Roux et al., 2017; Wagner et al., 2018, among others). Some recent studies have also dealt with this question using a modeling approach (Bense et al., 2012; Genxu et al., 2017; Burke et al., 2020; Du et al., 2020; Fabre et al., 2017, among others).

Bryophytes (mosses) and lichens are widely present in tundra and taiga environments. Dominant ground cover consists of *Sphagnum* mosses and lichens in permafrost peatlands (Soudzilovskaia et al., 2013; Volkova et al., 2018). *Sphagnum* mosses are part of the *Bryophyta* plant division, which represents non-vascular plants (without xylem or phloem). *Sphagnum* colonies grow indeterminately from their apical structure, named the *capitula*. Their water content mainly relies on capillary forces maintained by each individual's density (Hayward & Clymo, 1982; Howie & Hebda, 2018). Lichens are not

‘vegetation’ but consist of a symbiotic association between heterotrophic *Fungi* and autotrophic *Algae*. Both *Sphagnum* and lichens can be gathered into the *Cryptogamae* subkingdom. This cryptogamic layer has an important impact on permafrost dynamics because it influences heat and water exchanges between the soil and atmosphere (Soudzilovskaia et al., 2013; Launiainen et al., 2015; Porada et al., 2016; Park et al., 2018; Loranty et al., 2018). Boreal vegetation is assumed to be a major nutrient and inorganic solute exchange medium at a watershed scale (Shirokova et al., 2021). Boreal vegetation is likely to accumulate in lowlands at a low degradation rate, resulting in the formation of *Sphagnum* peatlands, such as the Western Siberian Lowlands.

Ground vegetation transfer properties are key information for high resolution hydrological modeling of permafrost-related catchments. Thus, reliable estimates of them are necessary for water flux studies for boreal soils and for climate change impact assessment on the hydrology of high latitude continental surfaces. Therefore, some recent efforts have been put to emphasize the role of the cryptogamic layer in Earth System Models (Stepanenko et al., 2020; Shi et al., 2021). Devoted modeling tools have also been created to predict *Sphagnum* dynamics (*Peatland Moss Simulator* by Gong et al., 2020). Furthermore, specific modeling work has been conducted on restored *Sphagnum* peatlands, to link hydrological properties with dissolved organic carbon dynamics (Bernard-Jannin et al., 2018) or soil moisture dynamics (Elliott & Price, 2020). However, the mechanistic modeling of water and heat fluxes in ground vegetation layers remains difficult, as their porous media transfer properties are not straightforward to evaluate (Orgogozo et al., 2019).

Many studies are available for the decayed *Sphagnum* layer: peat. The hydrological and thermal properties of peat are well documented. Extensive reviews of the relation between hydrogeochemical processes in peatlands and peat’s porous medium structure were conducted by McCarter et al. (2020). A study of peatland’s hydraulic properties was initiated during the 1920s, for peatland drainage (Malmström, 1925). Then, some introductory field experiments were conducted on Finnish peatlands (Virta, 1962; Heikurainen, 1963; Sarasto, 1963) as well as in the United States (Boelter, 1968) and Ireland (Galvin, 1976).

Only a few studies were conducted on the living part of this upper permafrost layer. Hence, quantitative assessments of some key hydrological properties of ground vegetation layers are needed, such as total, open and enclosed porosity, hydraulic conductivity and specific surface area. In terms of hydraulic properties, hydraulic conductivity has been assessed in the laboratory using constant or falling-head permeameters (Quinton et al., 2000; Price et al., 2008; Hamamoto et al., 2016; Weber et al., 2017) or via field measurements (Päivänen, 1973; Crockett et al., 2016; this study). The results are presented in Table 2, with some peat results for comparison. Otherwise, arctic lichens have received little attention, to date. To our knowledge, only one study has estimated lichens’ hydraulic properties, considering unsaturated hydraulic conductivity without taking into account macropores (Voortman et al., 2014). However, the specific surface areas of some other lichen species are documented in the literature (Adamo et al., 2007). Some studies quantified arctic lichen properties in response to

acid rain (Tarhanen et al., 1999), to clarify their interaction with the rhizosphere (Banfield et al., 1999), or in relation to their albedo properties (Bernier et al., 2011). Some transmembrane transfer properties are also available in the literature (Potkay et al., 2020)

105 Thus, many field and experimental studies are available throughout the literature. However, field work and experimental studies are known to bring their own difficulties, due to the local conditions variabilities, sampling biases, disturbances and measurement uncertainties. The aim of this study is to assess some of the transfer properties that are well documented with field and experimental studies with an innovative numerical scheme. Indeed, the use of numerical workflows enhance reproducibility and inter-comparisons capability between samples. Numerical workflows are often used when experimental studies are complicated to implement (reservoir engineering, aerodynamics, micro-fluidics).

110 In this work, such numerical workflow is intended to be used for evaluating the hydrological transfer properties of representative vegetation types of the Western Siberian Lowlands. To this end, natural samples collected from the Western Siberian Lowlands are digitally analyzed to characterize some morphological and hydraulic transfer properties. Thus, contrary to previous works compiled in Table 2, this study aims to assess the hydraulic properties of lichens and *Sphagnum* mosses by numerical methods rather than experimental measurements. The arctic cryptogamic layer is assumed, hereafter, to represent a complex patch work of biological porous media (Price et al., 2008, Voortman et al., 2014, Hamamoto et al., 2015).

Table 2 location

120 To validate this hypothesis, a thorough analysis of sample homogeneity is carried out, based on porosity, as it is the main driver of flow dynamics in porous media (Koponen et al., 1997, Koponen et al., 1996). This enables the classification of samples according to their homogeneity. Indeed, for homogeneous samples, a smaller sample region can be considered as an effective medium sharing the same properties as the whole sample. Multidimensional porosity description leads to a statistical study of the existence of a Representative Elementary Volume (REV). Two standard porous media modeling methodologies are used throughout this study: Direct Numerical Simulations on computed Representative Elementary Volumes (DNS-REV) and Pore Network Modeling with built-in solver (PNM). The impossibility to collect a substantial number of samples is compensated by a statistical quantification of a REV for each sample. This implies that the REV is smaller than the sample, hence sampling size is chosen to match sizes that were used in previous literature, such as Weber et al. (2017).

2. Material & Methods

2.1 Sample collection and digital reconstruction

Samples are collected at Khanymei Research Station (N63°43'19,73" E75°57'47,91") in Western Siberia (Autonomous District of Yamal-Nenets, Russian Federation) in July 2018. The mean annual temperature is -5.6 °C and average precipitation is 540 mm (Payandi-Rolland et al, 2020; Raudina et al., 2018). Eight moss samples (*Sphagnum sp.*) are collected, either on moss mounds or in thermokarstic hollows. Additionally, two lichen samples (*Cladonia sp.*, named Lichen1.3 and Lichen2.1) and two peat samples (named Peat2.2 and Peat2.3) are collected. Of the eight *Sphagnum* samples, three are *S. angustifolium* (C.E.O. Jensen ex Russow, named Mound2.4, Mound2.5 and Mound2.6), two are *S. lindbergii* Schimp (named Hollow1.2 and Hollow1.4) and two are *S. majus* (Russow) (C.E.O. Jensen, named Hollow2.7 and Hollow2.8). The last moss sample is *S. lenense* H. Lindb. ex L.I. Savicz (named Mound1.1).

Sampling is thoroughly conducted, to minimize structural perturbations. In order to achieve this, each sample's surroundings is cleared with special care prior to extraction. Then, the sample is extracted using a ceramic knife, directly at the right dimensions to fit in a high-density polyethylene box, where it remains from the moment of sampling and drying to the tomographic examination. Additionally, four in-situ hydraulic conductivity measurements are performed on various *Sphagnum* plots, using a double-ring infiltrometer (Table 2). An overview of the sample collection method is shown in Fig. 1, as well as 3D tomographical visualizations of each sample type.

Figure 1 location

The samples are then dried at 40 °C for 48 hours after sampling. Thereafter, each sample is scanned and digitally reconstructed using high resolution X-ray imagery.

X-ray Computed Tomography (X-CT) has been widely studied and is extensively used for medical purposes and geoscientific applications (Christe et al., 2011). Tomography is a non-destructive technique which enables the observation of pore structure data at micron scale, especially for pore space assessment in sedimentary rocks. X-CT scanning has been acknowledged as being an efficient method for accessing morphological information, such as the pore structure of peat soils (Turberg et al., 2014). Cnudde and Boone (2013) published an exhaustive review of X-ray tomography applications for earth sciences. Rezanezhad et al. (2016) demonstrated that X-CT peat scanning showed a satisfactory spatial resolution for the study of peat's pore morphology. Since bryophytes can be assumed to represent a cluster of individuals, X-CT permits the segmenting of each plant structure, which cannot otherwise be achieved without destructive techniques. Tomographical scans of studied samples are produced using an EasyTom® XL (RX Solutions, France) with a maximal X-ray emission source set to 90 kV. The obtained resolutions, after tridimensional reconstruction, is 94 $\mu\text{m}\cdot\text{voxel}^{-1}$, except for 'Lichen2.1' at 88 $\mu\text{m}\cdot\text{voxel}^{-1}$ (due to the scanning settings used specifically for this sample). The voxel number ranges from $4.8\cdot 10^8$ voxels to $9.6\cdot 10^8$ voxels. Virtual samples are cropped and reduced to form a Usable Volume (UV) to avoid sampling border effects.

Using ImageJ – Fiji (Schindelin et al., 2012), computed samples are then binarized using an intra-class variance reducing
165 algorithm (Otsu, 1979). This resulted in a sample consisting of an eight-bit black and white image stack. Supplement S1
contains some of the technical data, such as Usable Volumes and digital reconstructions, for each sample.

2.2 Drying impacts assessment on sample representativity

The sampling locations and processing facilities were far away from each other. To ensure structural preservation, special
care is taken throughout the sampling, transportation and scanning operations. The samples are oven-dried for 48 hours at 40
170 °C, at atmospheric pressure, to halt biological degradation. As expected, *Sphagnum* mosses began to whiten and become
papery, as described by Hayward & Clymo (1982). The samples are scanned at the Toulouse Institute of Fluid Mechanics in
dry conditions, two months after their primary extraction at Khanymei Research Station and drying.

To ensure the dry samples' representativity, we used an analogous drying experimental protocol than the one carried out by
175 Kämäräinen et al. (2018). This experiment is conducted on similar *Sphagnum* species (*S. fuscum* (Schimp.) H.Klinggr., *S.*
majus (Russow) C.E.O. Jensen) and sampled according to the same method at Clarens mire (Southwest France, N
43°08'41.3", E 0°25'12.9") in March 2021, notwithstanding that *Sphagnum* acrotelm (growing section of a *Sphagnum*
individual) is much thinner than Siberian samples. Four samples are collected, two being dried at 40 °C for 48 hours and the
other two being left untouched, as control samples. Each of the four samples are scanned two days after their extraction and
180 then again, 14 days after extraction. Additionally, one *Sphagnum majus* individual is extracted and left to dry in ambient
conditions.

A comparative study between each of the two sample lots and the lone individual show that drying does not affect structural
preservation. Our validation experiment converges with the results found by Kämäräinen et al. (2018). This also confirms
185 hyaline cells' structural durability; the early work of Puustjärvi (1977) showed that hyaline cells were well-preserved during
biological decay. Drying impacts aside, *Sphagnum*'s continuous growth on non-dried control samples seems the most
impactful structural factor, as each individual was striving to adapt itself to the sampling box' hydric conditions. Fast drying
before tomographic examination can be a reasonable solution for preserving the morphological structure, in conjunction with
careful on-site sampling.

190 2.3 Morphological analysis: Total porosity (ϵ_{total}), open porosity (ϵ_{open}), Specific Surface Area S_{SA} and Pore size distribution

Global porosity (ϵ_{Total}) is calculated for each sample using built-in ImageJ-Fiji's tools and macro scripting. Porosity is
considered to be a ratio between the number of voxels representing the void phase i_{voxel} (void phase's internal volume,
including closed porosity) over the total number of voxels representing a sample N_{total} (void and matrix volume). This
195 relation is shown in Eq. (1):

$$\epsilon_{Total} = \frac{V_{i=0}}{V_{Total}} \times 100 = \frac{\int_0^{N_{i=0}} \int_0^{N_{Total}} \int_0^{N_{Total}} i_{voxel}(x, y, z) dx dy dz}{\int_0^{N_{Total}} \int_0^{N_{Total}} \int_0^{N_{Total}} i_{voxel}(x, y, z) dx dy dz} \times 100 = \frac{\sum_0^{N_{i=0}} i_{voxel}}{\sum_0^{N_{Total}} i_{voxel}} \times 100, \quad (1)$$

Porosity is computed on bi-dimensional horizontal slices along the z axis to evaluate porosity variations along the samples.

200 Image stacks are then reconstructed along the x and y axis, to create two other image stacks. Finally, porosity is computed along the x , y and z axis using a voxel counting algorithm, shown in 3.1.

The samples could then be classified into three types, according to the porosity profile along the vertical axis (Table 3 and Supplement S2). As porosity appears to be almost constant over the x and y axis, sample classification is solely based on vertical porosity z :

- 205
- Type I: Constant high porosity along z axis excluding border effects;
 - Type II: Low basal porosity, linearly increasing to the top of the sample;
 - Type III: No specific trend observed on vertical porosity.

For each sample nature as well as each classified type, a dedicated color palette is choosen and kept consistent throughout the study for the sake of clarity.

210 Open and connected porosity (ϵ_{open}) are retrieved using dedicated shape analysis and labeling tools provided in the IPSDK™ image processing toolkit (a Reactiv'IP product, used in Goubet et al., 2021). This enables a precise segmentation to associate each connected void space into a unique identifier. Here, since the samples have more void than matter, this first label is assumed to be connected void space, which plays a major role in the flow and transfers (porosity), the latter being a closed or non-communicating element. From the raw dataset, voxel intensity is integrated to get the first label's voxel sum divided by the overall voxel number, as shown in Eq. (2):

$$p_{open} = \frac{\epsilon_{open}}{\epsilon_{Total}} = \frac{\sum_0^{N_{i \in label 0}} i_{voxel}}{\sum_0^{N_{Total}} i_{voxel}} \times \epsilon_{Total}^{-1}, \quad (2)$$

220 The specific surface area is deduced using the same shape analysis and labeling tools included in IPSDK™. Integrating the surface between both phases (void and solid) yields the total surface S . Thus, volumetric specific surface area S_{SA} is obtained by dividing this surface with the sample's bounding box volume, expressed in $\text{m}^2 \cdot \text{m}^{-3}$, as shown in Eq. (3):

$$S_{SA_v} = \frac{S_{solid}}{V_{BBox}} = \frac{\sum_{i=0}^{N-1} \sum_{j=0}^{N-1} S((i, j)(i+1, j+1))}{L_x L_y L_z}, \quad (3)$$

Specific surface area is conventionally expressed in relation to density (in $\text{m}^2 \cdot \text{g}^{-1}$). For this purpose, each dried sample mass is obtained using an analytical balance and the sample's dry bulk density ρ_{dry} . Then, volumetric specific surface values are converted into a mass-related specific surface by dividing volumetric specific surface area with dry density, as shown in Eq. (4):

$$S_{SA_m} = \frac{S_{SA_v}}{\rho_{dry}}, \quad (4)$$

Pore size distribution is calculated using ImageJ-Fiji's implemented image segmentation tools on the binarized image stacks. On each stack's image, a Euclidean distance transformation of the matrix phase from the void phase is first applied. Then, for each isolated void patch, the Feret diameter is computed.

235 2.4 Darcy scale morphological and hydrological properties' definition: Representative Elementary Volume (REV)

In this study, the collected samples are assumed to form a complex fibrous porous media. Resolving mechanistic equations in such large domains is not straightforward due to the extensive computational resources required. Conversely, resolving such equations on an arbitrary cropped sample would not aid the hydraulic property assessment. To make the link between microscale and macroscale phenomena, a reproducible pattern is required to avoid microscale heterogeneities and lack of information due to a diminutive sample size. To do this, finding a representative region that validates scale separation assumptions with both microscale and macroscale heterogeneities is compulsory, thus defining the volumetric average of a microscale property that is continuous and informative at a macroscale. One of the first volume averaging methods consists of finding a statistical Representative Elementary Volume (REV) for the given studied property.

Indeed, REV is a theoretical concept clarifying the definition of the macroscopic scale (Darcy scale) and the microscopic scale (pore scale) and characterizing a given porous medium. This REV can be assumed as a specific sample volume, in which transfer governing equations (single-phase flow, for example) may be defined, along with the associated effective properties. A proper mathematical definition of a REV is given in Bachmat and Bear (1987), Quintard and Whitaker (1989)

and Whitaker (1999), along with a thorough definition of volume averaging methods. A generic profile for a given property ϕ_p is shown in Fig. 2.

[Figure 2 location]

The fluctuation profile shows three main domains. Here, the REV is defined as the smallest volume for which statistical fluctuations of a given property in a given space are sufficiently low to consider its average value as an effective property. Finding the Representative Elementary Volumes of some key properties (e.g., porosity and intrinsic permeability) is a routine workflow in porous media sciences. It is often used for fractured oil reservoirs (Durlafsky, 1991) or artificially packed glass bead media (Leroy et al., 2008). A REV is, by definition, large if compared to characteristic lengths of heterogeneities at a microscopic scale but small if compared to characteristic lengths of heterogeneities at the macroscopic scale. Thus, the properties computed for a REV of a porous medium may be defined and computed as continuous functions of space and even constant, in the case of a homogeneous porous medium, as defined by Bear (1972). In general, REV's are described on the basis of morphological characteristics such as porosity, although a distinct REV can be found for any given porous media property. Porosity and hydraulic conductivity related REV's are characterized throughout this study, leading to two different sizes, one for each property.

2.4.1 Porosity: Binarization and voxel counting

From previously binarized image stacks, a statistical REV analysis is conducted using dedicated high performance image processing Python libraries (IPSDK™), encapsulated in a specifically designed batch process for which the flowchart is shown in Fig. 3.

[Figure 3 location]

First, porosity (Eq. 1) is computed for a given sub-sampling volume within the whole sample. Then, the sub-sampling volume location is incrementally reduced and moved in every spatial direction. For each sub-volume, intermediate porosities are computed. The average and standard deviation are stored for each chosen sub-sampling volume. Then, an algorithmic routine is used to find the maximal size that satisfies a given threshold (1, 3 or 5% of porosity fluctuation). These thresholds define the statistical representativity of these REV's. Thus, a REV satisfying a one percent threshold can be assumed to be a high-grade REV, whereas the five-percent threshold corresponds to lower-grade REV's. For 10 of the 12 studied samples, a REV of porosity is found. The two remaining samples, Hollow1.2 and Peat2.2, do not exhibit a REV for the chosen thresholds. A collection of tridimensional reconstructions of the samples as well as some examples of REV for each sample are shown in Supplement S1. The graphical plots for each studied sample are available in Supplement S3. The black dot represents the smallest reached Representative Elementary Volume for each sample.

2.4.2 Hydraulic conductivity: Direct Numerical Simulation

Hydraulic conductivity is estimated through single-phase flow computations performed by solving Navier-Stokes equation in the pore space of the considered sample. The concept is to carry out the numerical simulation of fluid flow, reproducing the conditions occurring in a constant-head permeameter. Then, a sample's hydraulic conductivity is computed from the
285 obtained velocity field. A virtual constant-head permeameter is created by imposing a constant pressure on two opposite faces to one direction (inlet and outlet). Watertight wall boundary conditions are applied on other faces, as shown in a conceptual representation of the initial and boundary conditions available in Supplement S2.

Due to computation time limitations, the biggest studied sub-volume with this approach corresponds to a quarter of the total
290 sample. In section 2.4, we stated that the REV of effective physical properties were valid for that particular physical property. Thus, a hydraulic conductivity REV is required, to statistically assess hydraulic conductivity. For that purpose, instead of counting voxel value algorithms (as made for porosity), retrieving a Representative Elementary Volume for hydraulic conductivity requires extensive fluid mechanics simulations. Here, a laminar single-phase flow induced by a pressure gradient is computed for each sub-sample, being consistent with the idea of reducing and moving a defined sub-
295 volume inside the overall sample. From open porosity data in Table 3, we can show that most porosity is connected to each one. This leads to the assumption that considering that all pores can be considered effective in permeability-driven phenomena. As these simulations are resource-costly, Type I samples (constant porosity) are selected as they are sufficiently homogeneous for the establishment of REV. Other types are treated by another method presented in 2.4.3. The implemented method relies on Mohammadmoradi & Kantzas (2016), in conjunction with automatic mesh manipulation tools (*trimesh*
300 Python library, Dawson-Haggerty et al., 2019). For each Type I sample, single-phase flow simulation through a fraction of the solid volume (representing a sample) is conducted. The *simpleFoam* algorithm is used to solve velocity field from an initial pressure gradient. The *simpleFoam* solver is an enhanced version on the original SIMPLE algorithm (*Semi-Implicit Method for Pressure-Linked Equations* - Patankar, 1980) nested in the open-source Computational Fluid Dynamics toolkit OpenFOAM (Weller et al., 1998, www.openfoam.org; www.openfoam.com).

305 For each sample, four potential REV sizes are computed (23.5 mm, 15.7 mm, 11.8 mm and 9.4 mm), consisting of 8, 27, 64 and 125 simulations on the x , y and z axis, respectively, representing 672 simulations per sample. These sizes are chosen from the beginning to limit computation times, as using the same scanning method than what was developed for porosity is computationnally-prohibitive. This is run on the tier-2 supercomputer *Olympe* (CALMIP computational mesocenter, Toulouse, France). These calculations are run simultaneously, each occupying one node (36 physical cores), representing
310 10,500 h CPU (about 12 days of physical time) per sample. For each simulation, the velocity field u_i is integrated with the overall outlet surface S_{outlet} (including the surface occupied by the solid matrix) to get an averaged outlet flux value v_i , according to Eq. (5):

$$v_i = \frac{1}{S_{outlet}} \int_0^S u_i dS,$$

315 (5)

A careful convergence study is also conducted so that numerical errors, associated with discretization resolutions and iterative procedures for the approximated inversions of the linear systems involved are low enough to be neglected in the analysis of the results. Inlet pressures are chosen to avoid turbulent flows ($Re \ll 1$). The computed Darcy velocity v_i could then be injected into a regular Darcy's law, as shown in Eq. (6), where k_{ii} is a tensorial component of intrinsic permeability (m²) and μ_w is the dynamic viscosity:

$$k_{ii} = v_i \frac{\mu_w}{\nabla P} \text{ with } \nabla P = \frac{P_{inlet} - P_{outlet}}{L_i},$$

(6)

To avoid artifacts related to the physics of a specific fluid, the *simpleFoam* solver uses kinematic pressure (expressed in m².s⁻²) and kinematic viscosity ν (in m².s⁻¹) to solve Navier-Stokes equations. These equations are based on intrinsic permeability k expressed in m². However, in the field of hydrology the hydraulic conductivity in m.s⁻¹, abbreviated to K_w , is generally used. One can relate hydraulic conductivity K_w to intrinsic permeability k by using Eq. (7) described by Claisse (2016).

$$k = \frac{K_w \mu_w}{\rho_w g},$$

(7)

In continental surface hydrology, liquid water's physical property variations (e.g., volumetric mass ρ_w and dynamic viscosity μ_w) are generally neglected. Thus, intrinsic permeability values obtained from the numerical computations were converted using water's thermodynamic properties at 293.15 K and 1.013 kPa (Chemical Rubber Company & Lide, 2004), considering the following conversion equation (Eq. (8)):

$$k = 1.0217 \cdot 10^{-7} K_w,$$

(8)

This method is suitable for samples meeting porosity homogeneity requirements, classified into Type I samples. However, another method is needed to compensate for Type II and Type III samples' heterogeneity, as using Direct Numerical Simulations on a complete Usable Volume is prohibitive, in terms of computational resources. The results obtained for hydraulic conductivity REV computations are available in Supplement S4.

A double-ring infiltrometry test was also conducted during the sampling campaign. For the sake of comparison, hydraulic conductivity values obtained using this method are also showed in Table

345

2.4.3 No REV for hydraulic conductivity: use of Pore Network Modeling (PNM)

For the samples that do not exhibit a REV for hydraulic conductivity (Type II and Type III samples), the hydraulic conductivity is then studied using a Pore Network model, generated from the binarized image stacks. Pore Network models are based on the structural simplification of a complex pore structure (rocks or reactive porous industrial media, for example) into a two-state model: spheres and throats. This method often uses various image processing and segmentation tools to generate a network of spheres and linking throats, based on an initial tridimensional volume. Introduced by Fatt (1956), pore network modelling was first studied in conjunction with predefined network properties. Then, pore network generation was adapted to model some porous media, scanned with X-ray tomography using image processing algorithms, as accurately as possible (Dong & Blunt, 2009, among others). Various algorithms are used to create the internal pore network structure, such as the *maximal ball* algorithm (Silin & Patzek, 2006). More recently, other algorithms based on the morphological properties of the studied porous media have emerged, such as the *Sub-Network of the Oversegmented Watershed (SNOW)* algorithm (Gostick, 2017). This alternative algorithm is considered to be computationally efficient, allowing a porous medium to be accurately modeled by numerical imagery (Khan et al., 2020). The SNOW algorithm showed a good fit with the standard *maximal ball* algorithm. Generating a pore network and simulating a flow in it is often cheaper, in terms of computational resources, when compared to Direct Numerical Simulation. However, more complex transfer mechanisms, such as imbibition and drainage, are still in the study phase and some extensive work on computational optimization has yet to be conducted, specifically on non-user-generated porous media (Maalal et al., 2021).

For each binarized type II and type III image stack, a direct pore network extraction is conducted using the SNOW algorithm, implemented in the *OpenPNM* and *PoreSpy* open-source Python libraries (Gostick et al., 2019). Then, a synthetic porosity and a synthetic specific surface area may be computed for the obtained simplified representation of the pore space of the porous medium. Using the implemented Stokes' equation solver, a diagonal permeability tensor is retrieved from the generated pore networks, applying the identical boundary conditions, based on the method given by Sadeghi & Gostick (2020). Once again, intrinsic permeability tensors are converted into a hydraulic conductivity tensor using the relation in Eq. (8).

In Supplement S5, a comparative study is described, based on Type I samples between both developed workflows. Then, some clues are given as to whether Direct Numerical Simulation (DNS) or Pore Network Modeling (PNM) is suitable for a given sample.

3.1 Morphological analysis

The global porosity and open porosity proportion (p_{open}) for each sample is shown in Table 3, ranging from less than 40 % (Mound1.1) to more than 95% (Hollow2.7).

380 [Table 3 location]

On average, lichens are the most porous of the collection and peat is the least porous. Porosity values are in line with previously obtained data from the literature, for the highest porous media of the collection (Yi et al., 2009). However, an important variability can be observed for *Sphagnum* samples, gathering minimal and maximal porosity values. Mound
385 mosses have an average porosity of $65.9 \pm 22.3\%$, whereas, average hollow moss sample porosity is $79.6 \pm 20.2\%$. Porosity profiles for each sample are presented in Fig. 4.

[Figure 4 location]

390 No specific trend can be accessed from the x and y axes porosity profiles and yet, variations can be observed on the z axis. Again, three trends can be observed, clustering samples into three groups according to their respective porosity profile trends:

- Type I: Stable high porosity profile samples, excluding border effects ($\epsilon_{total} > 80\%$): Mound2.6, Hollow2.7, Hollow2.8, Lichen2.1, Lichen1.3;
- 395 ▪ Type II: Medium high porosity profile samples associated with a progressive increase from the bottom to the top: Hollow1.2, Hollow1.4, Peat2.2, Peat2.3; and
- Type III: Medium low porosity associated with no specific trend porosity profiles: Mound1.1, Mound2.4, Mound2.5.

Type I class contains both lichen samples (Lichen2.1, Lichen1.3) whereas type III only consists of mound *Sphagnum*
400 (Mound1.1, Mound2.4, Mound2.5). Type II class contains half of the hollow *Sphagnum* samples, as well as both peat samples (Peat2.2, Peat2.3).

Open and connected porosity (p_{open} , Table 3) represents nearly all the void space volume in each sample. Open porosity ratio values range from 0.99 to 0.9999. Thus, we can assume that, due to the fibrous nature of the studied material, enclosed
405 porosity is not playing a major role in the flow dynamics of the studied samples.

Pore size distribution (Fig. 5) is heterogeneous in each sample and the sizes are concentrated between 0.01 mm and 1.00 mm of pore radii. The median pore size varies from 0.23 mm (for peat samples) up to 0.88 mm (for lichen samples).

410 [Figure 5 location]

Intermediate median pore size values can be found for mound *Sphagnum* samples at average values between 0.34 mm and 0.70 mm (for hollow *Sphagnum* samples). According to the previous classification, the median pore size for each sample type (I, II and III) is 0.66 mm, 0.42 mm and 0.33 mm, respectively. While Type II and Type III curves differ in
415 bidimensional porosity along z , they share similar global pore size distributions. Type I samples are distinct from Type II and Type III curves. Specific Surface Area (S_{SA}) values for each sample are shown in Fig. 6.

[Figure 6 location]

420 Specific Surface Area values seem to be uneven between each sample type. For instance, low specific surface areas can be observed for some hollow *Sphagnum* samples ($2.6 \cdot 10^{-2} \text{ m}^2 \cdot \text{g}^{-1}$ and $2.9 \cdot 10^{-2} \text{ m}^2 \cdot \text{g}^{-1}$ for Hollow2.7 and Hollow2.8, respectively). Higher specific area values can be found for one mound of *Sphagnum* ($2.0 \cdot 10^{-2} \text{ m}^2 \cdot \text{g}^{-1}$ for Mound2.4) and for one hollow *Sphagnum* sample ($1.7 \cdot 10^{-1} \text{ m}^2 \cdot \text{g}^{-1}$ for Hollow1.2).

3.2 Porosity

425 Representative Elementary Volumes for porosity have been computed when possible. For samples exhibiting a REV, porosity has been computed using Eq. 1 applied to the REV. For samples admitting no REV, porosity has still been computed using Eq. 1, but applied to the whole usable volume of the sample. A REV retrieval algorithm was applied to all the twelve studied samples, although two of them (Hollow1.2 and Peat2.2) did not admit a REV. Obtained REV sizes are shown in Table 4. Some examples of tridimensional visualizations of REV's of Porosity are shown in Supplement S1. Due to
430 the numerous graphs obtained during REV computation, tridimensional porosity plots are available in Supplement S3.

[Table 4 location]

REV _{ϵ} sizes vary from 2 mm to 2 cm, representing $8.0 \cdot 10^3$ to $2.19 \cdot 10^6$ voxels. Substantial morphological variations are
435 visible, spanning from simple tubular structures (visible in the REV of Hollow2.7) to a complex and fibrous medium (for the Mound2.6 sample, Supplement S1). The average porosity obtained for these REV's (shown in Supplement S3) varies from 83.4% to 96.0%, which confirms the high porosity factor of these biological media. Computation times for porosity-REV retrieval ranges from three to six hours, using two Intel® Xeon® E5-2680 v2 (2.80 GHz) processors and 128 GB of RAM,

using high performance Python image processing libraries (IPSDK™). Graphical synthesis of the digital porosity assessment
440 is presented in Fig. 7.

[Figure 7 location]

3.3 Hydraulic conductivity

Due to the time and computational resources needed to achieve a careful study of a Representative Elementary Volume of
445 hydraulic conductivity, only Type I samples were studied by DNS, as they represent the most homogeneous samples of the
collection. Computed REV_κ of the hydraulic conductivity sizes are given in Table 5. Diagonal hydraulic conductivity tensor
components are shown in Fig. 8 and box plots are available in Supplement S4. Computations for the largest sub-sample size
(on a 23.5 mm edge), showed component hydraulic conductivity values than for the three smaller sizes. This discrepancy can
be related to an insufficient computation number for obtaining a good average value, hence a wider statistical spread around
450 the mean value. Moreover, the higher values for the largest studied sizes can also be correlated to heterogeneous hydraulic
conductivity behavior, as theoretically shown in Fig. 2, such as effects related to the existence of macropores. An example of
a pressure field obtained on a sub-sample of Hollow2.8 through DNS, is shown in Fig. 9-Right.

[Table 5 location]

455 For three of the Type I samples, REV_κ length is computed as 15.7 mm, which is the second largest computed size. Variations
in hydraulic conductivity, with respect to study volume reduction, are smaller than those found for porosity, although study
points were scarcer in the case of hydraulic conductivity assessment. Lichen1.3 shows the smallest REV_κ. It can be seen that
the smallest REV_ε was also described for Lichen1.3. Size differences can be seen between REV_ε and REV_κ, up to five times
460 larger for Lichen1.3 and half the REV_ε for Mound2.6. This seems to show that the Representative Elementary Volume found
for porosity cannot accurately describe properties such as hydraulic conductivity. This is often the case, as porosity REV is
smaller than the REV_κ defined for other properties (Zhang et al., 2000; Costanza-Robinson et al., 2011).

Numerical estimations of hydraulic conductivity are presented in Fig. 8. For each sample of Type I, the axial components of
465 the hydraulic conductivity tensor is given, based on the Representative Elementary Volume of hydraulic conductivity. For
Type II and Type III samples, hydraulic conductivity estimates are given, based on pore network modeling. An example of
pressure field computation is shown on sample Mound2.5 in Fig. 9-Left. Using a pore network allows the estimation of
properties in a model based on the whole sample. The use of a pore network is an affordable alternative to Direct Numerical
Simulations at the cost of accuracy.

470

[Figures 8 & 9 location]

The values obtained, vary from $1.1 \cdot 10^{-1} \text{ m.s}^{-1}$ to $9.5 \cdot 10^{-1} \text{ m.s}^{-1}$ for Type I samples and from $7.8 \cdot 10^{-3} \text{ m.s}^{-1}$ to $4.8 \cdot 10^{-1} \text{ m.s}^{-1}$ for Type II and III samples. Type I samples can be assumed to be highly water conductive biological media. Mean hydraulic conductivity decreases when the computed region size becomes smaller, for each direction and each sample (Supplement S4). *In-situ* measurements, conducted by infiltration (Table 2), give an average of 10^{-5} m.s^{-1} , which is in the same order of magnitude as previously published field measurements (Crockett et al., 2016) and computed values (McCarter & Price, 2012). Analogous values for vertical hydraulic conductivity have been found in the literature at $k_{zz} \approx 10^{-2} \text{ m.s}^{-1}$ (Päivänen, 1973; Crockett et al., 2016; Golubev et al., 2021). However, other studies showed results of a different order of magnitude for *Sphagnum* samples, with values under 10^{-4} m.s^{-1} (Hamamoto et al., 2015). These differences could be explained by the experimental method used to retrieve hydraulic conductivity, as well as *Sphagnum* bog oscillation occurring during sampling (*mire breathing*) (Strack et al., 2009; Golubev & Whittington, 2018; Howie & Hebda, 2018), which is going to be discussed in the next part.

4. Discussion

Digital assessments of the morphological and hydraulic properties of *Sphagnum* and lichens of the Western Siberian Lowlands presented in this work, suggest extremely porous, connected media with high specific surfaces and high hydraulic conductivities. These results are in line with the biogeochemical observations of Shirokova et al. (2021), demonstrating the overwhelming role of *Sphagnum* mosses in organic carbon, nutrient and inorganic solute fluxes in the Western Siberian Lowlands. Nonetheless, discrepancies between the numerical results presented in this work (Fig.7 and Fig. 8) and previously published measurements of the hydraulic properties of *Sphagnum* are noteworthy (Table 2). Weaker, but still sizeable, differences can be seen between the results given by both of the numerical methods used here for the estimation of hydraulic conductivity on the same sample, namely Direct Numerical Simulation (DNS) and Pore Network Modeling (PNM). This last methodological point is discussed in Supplement S5, where a comparative validation is performed between DNS and PNM on homogeneous samples (Type I).

4.1 Numerical reconstruction after scanning

Due to technical limitations, scanning devices have a minimal resolution that causes a loss of information, acting as a threshold. In this study, minimal resolution fluctuated between 88 and 94 $\mu\text{m.voxel}^{-1}$, meaning that two elements of this size could not be distinguished. In our study, technically unreachable porosity (porosity that is smaller than the minimal scanning resolution) is assumed to play a negligible role in transfers through a saturated medium, reacting as an enclosed porosity. Pre-processing algorithms (especially binarization) can cause information loss due to the arbitrary categorization of each voxel. This erroneous description can be seen for small elements (such as *Sphagnum* leaves) which shrink them. Mesh generation may also bring some additional ‘over-erosion’ that helps flows inside a sample. These impacts could be studied

by reducing scanning resolution, albeit not available at the time of the scans. However, hydraulic conductivity overestimation in DNS that could be related to these pre-processing effects is likely to be negligible. Indeed, the high porosities encountered and the preferential flow paths that occur in the largest pores (macro-pores) predominate over enclosed pore dynamics. This might not be the case for unsaturated hydraulic property assessments.

4.2 Numerical results vs. field experiments: porosity and specific surface

As described in previous sections of this study, the samples collected are considerably porous. Porosity values are in line with past results found in the literature (Yi et al., 2009; Kämäräinen et al., 2018), with porosities above 90% for some of the samples. Interestingly, volumetric digital specific surface can be well linked with the porosity of complete samples, as well as the average porosities found for Representative Elementary Volumes.

A clustering can be seen for the three studied sample types (Fig. 10), although mathematical relations between specific surface and porosity are not well-defined for such porous media. The specific surface values obtained are of the same magnitude as previous values obtained for other natural moss and lichen species, using geometrical calculations ($1.4 \cdot 10^{-1} \text{ m}^2 \cdot \text{g}^{-1}$ for *Hypnum cupressiforme* (Hedw., 1801) moss and $2.4 \cdot 10^{-2} \text{ m}^2 \cdot \text{g}^{-1}$ for *Pseudevernia furfuracea* ((L.) Zopf, 1903) lichen in Adamo et al., 2007). These values are still notably lower than the values obtained using the B.E.T. method of N_2 adsorption isotherms ($1.1 \cdot 10^1 \text{ m}^2 \cdot \text{g}^{-1}$ for artificially grown *Sphagnum denticulatum* (Brid., 1926) in Gonzalez et al., 2016). As discussed in Section 4.1, a lack of micropores could explain the observed discrepancies (one to two orders of magnitude) between calculated geometric and B.E.T.

[Figure 10 location]

4.3 Numerical results vs. field experiments: hydraulic conductivity

In Supplement S5, a comparison between Direct Numerical Simulations and Pore Network Modelling is made showing that Pore Network Modelling is suitable to bypass the heterogeneity issues observed in our samples. Indeed, the obtained porosity values with PNM are in a five-percent threshold, compared to voxel counting results (Eq. (1)). The hydraulic conductivities computed by PNM and DNS are more contrasted, with one to two orders of magnitude of difference. One should bear in mind that the range of hydraulic conductivity of natural porous media is huge, with up to fifteen orders of magnitude between coarse gravel ($10^{-1} \text{ m} \cdot \text{s}^{-1}$) and unweathered shale ($10^{-15} \text{ m} \cdot \text{s}^{-1}$). Besides this, it is logical that the simplifications involved in the PNM method result in information loss compared to the DNS method. On the other hand, computational time savings (by using the PNM method) are huge (counted in tenth of days for DNS and hours for PNM). In some cases, (e.g., samples of Type II and III) DNS is simply not possible with the current regional scale supercomputing means.

535 The obtained numerical hydraulic conductivities tend to show high, and relatively isotropic, hydraulic conductivity tensor values. Hydraulic conductivities found using Direct Numerical Simulations (DNS) are sizably higher than previous values found in the literature using field percolation (Table 2), often by up to one to three orders of magnitude. The hydraulic conductivities found using Pore Network Modeling seem to be more in line with the values in Table 2 as well as the field experiment results shown in Table 6. Nevertheless, it should be kept in mind that the results obtained by this method are less
540 structurally accurate than those obtained from DNS, since they rely on a simplified description of the pore structure. Some clues can be advanced to explain this discrepancy: the first being the impact of numerical reconstruction routines and mesh generation procedure (discussed in 4.1); the latter being moss compression during field experiments.

Table 6 location

545 Our digital, constant-head permeameter experiments were conducted in a fully saturated media. Technically unreachable porosity (porosity that is smaller than the minimal scanning resolution) is assumed to play a negligible role in transfers through a saturated medium, reacting as enclosed porosity. In the case of low permeability porous media, such sub-resolution porosity may affect flow (Soulaine et al., 2016). However, in the case of highly porous and connected media like mosses and
550 lichens, the effects related to sub-resolution porosity are assumed to be low, when compared to the effects of the large macropores, which has been shown by Baird (1997). It should also be noted that most of the porosity is opened and connected in our case.

However, moss and lichen samples are compressible (Golubev & Whittington, 2018; Howie & Hebda, 2018; Price &
555 Whittington, 2010). Field percolation experiments induce a sizeable and rapid mass imbalance on this bryophytic cover, compacting the pore space more than would occur in natural rainfall conditions. This might notably affect flow patterns in macro-pores and explain the lower hydraulic conductivities found in field experiments. Indeed, some clues are given with the results of Weber et al. (2017) on hydraulic conductivity variations according to water saturation. Therefore, the numerical hydraulic conductivity assessments carried out in this study enable property quantification of the medium without
560 perturbation, such as compression of the biological pore structure, which is not possible in field experiments.

5. Conclusions and perspectives

A numerical assessment of morphological and hydraulic properties was carried out on digital X-CT reconstructions of samples of *Sphagnum* moss, lichen and peat from the Western Siberian Lowlands' bryophytic cover. This porous media-centered approach confirmed the high porosities (from 70 to 95% for most samples) already found in previous studies
565 involving experimental measurements. Hydraulic conductivity estimation was conducted using Direct Numerical Simulations for Type I samples and Pore Network Modeling for Type II and III samples, both fluctuating around 10^{-1} m.s^{-1} .

Indeed, both methods used in this study converge to classify macroscopic lichen, *Sphagnum* moss and peat as being considerably porous and pervious biological media. Hydraulic conductivity tensor shows isotropic horizontal components, however, some differences can be seen, particularly on the vertical component. Both methods reach higher values than seen
570 before in the literature. This may have been caused by interfering phenomena, such as moss compressibility, occurring during field experiments.

The methods developed for this application show that a numerical workscheme based on image processing allows retrieving the morphological properties of any variety of sample. Using such method permits nearly unlimited number of properties
575 assessment on the same sample whereas an experimental workscheme requires many samples. Numerical methods enables a qualitative classification of the overall homogeneity of a sample, which is not easily doable using solely experimental methods. Image processing seems to be a satisfactory method, provided that the studied sample is sufficiently homogeneous for the studied property. For heterogeneous samples, image processing is not optimal. However, in the absence of another method, pore network modelling allows to obtain some information on the studied property which is close to the one found
580 for the homogeneous samples using image processing.

These results provide firm ground for quantitative hydrological modeling of the bryophytic cover in permafrost-dominated peatland catchments, which is crucially important for a better understanding of the global climate change impacts on arctic areas. Using numerical methods potentially enables the assessment of moss and lichen's structural hydraulic conductivity without disturbance by any biological or physical phenomena. Therefore, the porous medium approaches developed
585 throughout this study lead to unprecedented qualitative and quantitative descriptions of such peculiar, highly porous, biological media.

These physical properties can then be used as input parameters to describe ground vegetation layers in high resolution hydrological models of arctic hydro-systems and extensively refine simulations of this critical compartment of boreal
590 continental surfaces. For example, they will be used in further modeling studies of permafrost under climate change at the Khanymei Research station, in the framework of the HiPerBorea project (hiperborea.omp.eu). Further studies are needed to assess variable water content consequences on peat and vegetation pore structure. Indeed, water content is one of the main drivers controlling effective transport properties, such as unsaturated flow, volume change and thermal conductivity.

Acknowledgments

595 This work was supported by the French Research Agency (ANR) under the HiPerBorea project (High Performance computing for quantifying climate change in Boreal areas, grant ANR-19-CE46-0003-01), by the CNRS (BryoPhyGel project) and by the French embassy in Russia (PHC Kolmogorov project 2017 N° 38144TB). This work was granted access to the HPC resources of the CALMIP super-computing center, under the allocation 2020-[p12166]. Partial support from the

Tomsk State University Development Program («Priority-2030») is also acknowledged. S. Loiko and A. Lim thank the
600 Russian Science Foundation (project no. 18-77-10045) for supporting the field work, and Georgiy Istigechev for his help for
the double-ring infiltrometry. The authors thank L. Bernard and R. Abbal of Reactiv'IP for their support regarding the
developments of the digital characterizations with IPSDK™. The authors also want to thank the Clarens mire steering
committee (<http://tourbiere-clarens.n2000.fr/>) for giving us permission to collect samples.

605 References

- Aalto, J., Karjalainen, O., Hjort, J., and Luoto, M.: Statistical Forecasting of Current and Future Circum-Arctic Ground Temperatures and Active Layer Thickness, *Geophys. Res. Lett.*, 45, 4889–4898, <https://doi.org/10.1029/2018GL078007>, 2018.
- 610 Adamo, P., Crisafulli, P., Giordano, S., Minganti, V., Modenesi, P., Monaci, F., Pittao, E., Tretiach, M., and Bargagli, R.: Lichen and moss bags as monitoring devices in urban areas. Part II: Trace element content in living and dead biomonitors and comparison with synthetic materials, *Environmental Pollution*, 146, 392–399, <https://doi.org/10.1016/j.envpol.2006.03.047>, 2007.
- 615 Bachmat, Y. and Bear, J.: On the Concept and Size of a Representative Elementary Volume (Rev), in: *Advances in Transport Phenomena in Porous Media*, edited by: Bear, J. and Corapcioglu, M. Y., Springer Netherlands, Dordrecht, 3–20, https://doi.org/10.1007/978-94-009-3625-6_1, 1987.
- Baird, A.: Field estimation of macropore functioning and surface hydraulic conductivity in a fen peat, 3, 287–295, [https://doi.org/10.1002/\(SICI\)1099-1085\(19970315\)11:3<287::AID-HYP443>3.0.CO;2-L](https://doi.org/10.1002/(SICI)1099-1085(19970315)11:3<287::AID-HYP443>3.0.CO;2-L), 1997.
- 620 Banfield, J. F., Barker, W. W., Welch, S. A., and Taunton, A.: Biological impact on mineral dissolution: Application of the lichen model to understanding mineral weathering in the rhizosphere, *Proceedings of the National Academy of Sciences*, 96, 3404–3411, <https://doi.org/10.1073/pnas.96.7.3404>, 1999.
- 625 Bear, J.: *Dynamics of fluids in porous media*, Dover, New York, 764 pp., 1972.
- Bense, V. F., Kooi, H., Ferguson, G., and Read, T.: Permafrost degradation as a control on hydrogeological regime shifts in a warming climate: GROUNDWATER AND DEGRADING PERMAFROST, *J. Geophys. Res.*, 117, n/a-n/a, <https://doi.org/10.1029/2011JF002143>, 2012.
- 630 Bernard-Jannin, L., Binet, S., Gogo, S., Leroy, F., Défarge, C., Jozja, N., Zocatelli, R., Perdereau, L., and Laggoun-Défarge, F.: Hydrological control of dissolved organic carbon dynamics in a rehabilitated *Sphagnum*-dominated peatland: a water-table based modelling approach, *Hydrol. Earth Syst. Sci.*, 22, 4907–4920, <https://doi.org/10.5194/hess-22-4907-2018>, 2018.
- Bernier, P. Y., Desjardins, R. L., Karimi-Zindashty, Y., Worth, D., Beaudoin, A., Luo, Y., and Wang, S.: Boreal lichen woodlands: A possible negative feedback to climate change in eastern North America, *Agricultural and Forest Meteorology*, 151, 521–528, <https://doi.org/10.1016/j.agrformet.2010.12.013>, 2011.
- Biskaborn, B. K., Smith, S. L., Noetzli, J., Matthes, H., Vieira, G., Streletskiy, D. A., Schoeneich, P., Romanovsky, V. E., Lewkowicz, A. G., Abramov, A., Allard, M., Boike, J., Cable, W. L., Christiansen, H. H., Delaloye, R., Diekmann, B.,

- 640 Drozdov, D., Etzelmüller, B., Grosse, G., Guglielmin, M., Ingeman-Nielsen, T., Isaksen, K., Ishikawa, M., Johansson, M.,
Johannsson, H., Joo, A., Kaverin, D., Kholodov, A., Konstantinov, P., Kröger, T., Lambiel, C., Lanckman, J.-P., Luo, D.,
Malkova, G., Meiklejohn, I., Moskalenko, N., Oliva, M., Phillips, M., Ramos, M., Sannel, A. B. K., Sergeev, D., Seybold,
C., Skryabin, P., Vasiliev, A., Wu, Q., Yoshikawa, K., Zheleznyak, M., and Lantuit, H.: Permafrost is warming at a global
scale, *Nat Commun*, 10, 264, <https://doi.org/10.1038/s41467-018-08240-4>, 2019.
- 645 Boelter, D. H.: Important Physical Properties of Peat Materials, 3rd International Peat Congress, Quebec, Cananada, 150–
154, 1968.
- Brown, G. O. and Hsieh, H. T.: Evaluation of laboratory dolomite core sample size using representative elementary volume
650 concepts, 36, 1199–1207, <https://doi.org/10.1029/2000WR900017>, 2000.
- Brown, J., Ferrians, O. J., Heginbottom, J. A. Jr., and Melnikov, E. S.: Circum-arctic map of permafrost and ground-ice
conditions, USGS, 1997.
- 655 Burke, E. J., Zhang, Y., and Krinner, G.: Evaluating permafrost physics in the Coupled Model Intercomparison Project 6
(CMIP6) models and their sensitivity to climate change, *The Cryosphere*, 14, 3155–3174, [https://doi.org/10.5194/tc-14-
3155-2020](https://doi.org/10.5194/tc-14-3155-2020), 2020.
- Chemical Rubber Company and Lide, D. R. (Eds.): CRC handbook of chemistry and physics: a ready-reference book of
660 chemical and physical data, 85. ed., CRC Press, Boca Raton, 2004.
- Christe, P., Turberg, P., Labiouse, V., Meuli, R., and Parriaux, A.: An X-ray computed tomography-based index to
characterize the quality of cataclastic carbonate rock samples, *Engineering Geology*, 117, 180–188,
<https://doi.org/10.1016/j.enggeo.2010.10.016>, 2011.
- 665 Claisse, P. A.: Transport of fluids in solids, in: *Civil Engineering Materials*, Elsevier, 83–90, [https://doi.org/10.1016/B978-0-
08-100275-9.00009-7](https://doi.org/10.1016/B978-0-08-100275-9.00009-7), 2016.
- Clayton, L. K., Schaefer, K., Battaglia, M. J., Bourgeau-Chavez, L., Chen, J., Chen, R. H., Chen, A., Bakian-Dogaheh, K.,
670 Grelik, S., Jafarov, E., Liu, L., Michaelides, R. J., Moghaddam, M., Parsekian, A. D., Rocha, A. V., Schaefer, S. R.,
Sullivan, T., Tabatabaenejad, A., Wang, K., Wilson, C. J., Zebker, H. A., Zhang, T., and Zhao, Y.: Active layer thickness as
a function of soil water content, *Environ. Res. Lett.*, 16, 055028, <https://doi.org/10.1088/1748-9326/abfa4c>, 2021.
- Cnudde, V. and Boone, M. N.: High-resolution X-ray computed tomography in geosciences: A review of the current
675 technology and applications, *Earth-Science Reviews*, 123, 1–17, <https://doi.org/10.1016/j.earscirev.2013.04.003>, 2013.

Costanza-Robinson, M. S., Estabrook, B. D., and Fouhey, D. F.: Representative elementary volume estimation for porosity, moisture saturation, and air-water interfacial areas in unsaturated porous media: Data quality implications: REV ESTIMATION, *Water Resour. Res.*, 47, <https://doi.org/10.1029/2010WR009655>, 2011.

680 Crockett, A. C., Ronayne, M. J., and Cooper, D. J.: Relationships between vegetation type, peat hydraulic conductivity, and water table dynamics in mountain fens: Relating Vegetation Type and Peat Hydraulic Conductivity in Mountain Fens, *Ecohydrol.*, 9, 1028–1038, <https://doi.org/10.1002/eco.1706>, 2016.

685 Dawson-Haggerty et al.: trimesh, 2019.

Dong, H. and Blunt, M. J.: Pore-network extraction from micro-computerized-tomography images, *Phys. Rev. E*, 80, 036307, <https://doi.org/10.1103/PhysRevE.80.036307>, 2009.

690 Du, X., Loisel, D., Alessi, D. S., and Faramarzi, M.: Hydro-climate and biogeochemical processes control watershed organic carbon inflows: Development of an in-stream organic carbon module coupled with a process-based hydrologic model, *Science of The Total Environment*, 718, 137281, <https://doi.org/10.1016/j.scitotenv.2020.137281>, 2020.

Durlofsky, L. J.: Numerical calculation of equivalent grid block permeability tensors for heterogeneous porous media, *Water*
695 *Resour. Res.*, 27, 699–708, <https://doi.org/10.1029/91WR00107>, 1991.

Elliott, J. and Price, J.: Comparison of soil hydraulic properties estimated from steady-state experiments and transient field observations through simulating soil moisture in regenerated Sphagnum moss, *Journal of Hydrology*, 582, 124489, <https://doi.org/10.1016/j.jhydrol.2019.124489>, 2020.

700 Fabre, C., Sauvage, S., Tananaev, N., Srinivasan, R., Teisserenc, R., and Sánchez Pérez, J.: Using Modeling Tools to Better Understand Permafrost Hydrology, *Water*, 9, 418, <https://doi.org/10.3390/w9060418>, 2017.

Fatt, I.: The Network Model of Porous Media, 207, 144–181, <https://doi.org/10.2118/574-G>, 1956.

705

- Fox-Kemper, B., Hewitt, H. T., Xiao, C., Aðalgeirsdóttir, G., Drijfhout, S. S., Edwards, T. L., Golledge, N. R., Hemer, M., Kopp, R. E., Krinner, G., Mix, A., Notz, D., Nowicki, S., Nurhati, I. S., Ruiz, L., Sallée, J. B., Slangen, A. B. A., and Yu, Y.: Ocean, Cryosphere and Sea Level Change., in: Climate Change 2021: The Physical Science Basis. Contribution of Working Group I to the Sixth Assessment Report of the Intergovernmental Panel on Climate Change, edited by: Masson-Delmotte, V., Zhai, V. P., Pirani, A., Connors, S. L., Péan, C., Berger, S., Caud, N., Chen, Y., Goldfarb, L., Gomis, M. I., Huang, M., Leitzell, K., Lonnoy, E., Matthews, J. B. R., Maycock, T. K., Waterfield, T., Yelekçi, O., Yu, R., and Zhou, B., Cambridge University Press., In Press.
- Galvin, L.: Physical properties of Irish peats, 207–221, 1976.
- Genxu, W., Tianxu, M., Juan, C., Chunlin, S., and Kewei, H.: Processes of runoff generation operating during the spring and autumn seasons in a permafrost catchment on semi-arid plateaus, Journal of Hydrology, 550, 307–317, <https://doi.org/10.1016/j.jhydrol.2017.05.020>, 2017.
- Golubev, V. and Whittington, P.: Effects of volume change on the unsaturated hydraulic conductivity of Sphagnum moss, Journal of Hydrology, 559, 884–894, <https://doi.org/10.1016/j.jhydrol.2018.02.083>, 2018.
- Golubev, V., McCarter, C., and Whittington, P.: Ecohydrological implications of the variability of soil hydrophysical properties between two Sphagnum moss microforms and the impact of different sample heights, Journal of Hydrology, 603, 126956, <https://doi.org/10.1016/j.jhydrol.2021.126956>, 2021.
- Gong, J., Roulet, N., Frolking, S., Peltola, H., Laine, A. M., Kokkonen, N., and Tuittila, E.-S.: Modelling the habitat preference of two key *Sphagnum* species in a poor fen as controlled by capitulum water content, Biogeosciences, 17, 5693–5719, <https://doi.org/10.5194/bg-17-5693-2020>, 2020.
- Gonzalez, A. G., Pokrovsky, O. S., Beike, A. K., Reski, R., Di Palma, A., Adamo, P., Giordano, S., and Angel Fernandez, J.: Metal and proton adsorption capacities of natural and cloned Sphagnum mosses, Journal of Colloid and Interface Science, 461, 326–334, <https://doi.org/10.1016/j.jcis.2015.09.012>, 2016.
- Gostick, J., Zohaib-Atiq, Tranter, T., Lam, M., Sadeghi, A., Mdrkok, Weber, B. W., Sreeyuth Lal, and Day, R.: PMEAL/porespy: New features and bug fixes, <https://doi.org/10.5281/ZENODO.2633284>, 2019.
- Gostick, J. T.: Versatile and efficient pore network extraction method using marker-based watershed segmentation, Phys. Rev. E, 96, 023307, <https://doi.org/10.1103/PhysRevE.96.023307>, 2017.
- Goubet, M., Matei, C., Saghi, Z., Viala, B., and Tortai, J.-H.: 3D multi-scale study on metal/polymer nano-composites, Microsc Microanal, 27, 1766–1768, <https://doi.org/10.1017/S1431927621006462>, 2021.

- Grenier, C., Anbergen, H., Bense, V., Chanzy, Q., Coon, E., Collier, N., Costard, F., Ferry, M., Frampton, A., Frederick, J.,
745 Gonçalves, J., Holmén, J., Jost, A., Kokh, S., Kurylyk, B., McKenzie, J., Molson, J., Mouche, E., Orgogozo, L., Pannetier,
R., Rivière, A., Roux, N., Rühaak, W., Scheidegger, J., Selroos, J.-O., Therrien, R., Vidstrand, P., and Voss, C.:
Groundwater flow and heat transport for systems undergoing freeze-thaw: Intercomparison of numerical simulators for 2D
test cases, *Advances in Water Resources*, 114, 196–218, <https://doi.org/10.1016/j.advwatres.2018.02.001>, 2018.
- Guo, D. and Wang, H.: Simulated Historical (1901-2010) Changes in the Permafrost Extent and Active Layer Thickness in
750 the Northern Hemisphere: Historical Permafrost Change, *J. Geophys. Res. Atmos.*, 122, 12,285-12,295,
<https://doi.org/10.1002/2017JD027691>, 2017.
- Hamamoto, S., Dissanayaka, S. H., Kawamoto, K., Nagata, O., Komatsu, T., and Moldrup, P.: Transport properties and
755 pore-network structure in variably-saturated *Sphagnum* peat soil: Mass transport properties for peat soil, *Eur J Soil Sci*, 67,
121–131, <https://doi.org/10.1111/ejss.12312>, 2016.
- Hayward, P. M. and Clymo, R. S.: Profiles of water content and pore size in *Sphagnum* and peat, and their relation to peat
bog ecology, *Proc. R. Soc. Lond. B.*, 215, 299–325, <https://doi.org/10.1098/rspb.1982.0044>, 1982.
- 760 Heikurainen, L.: On using ground water table fluctuations for measuring evapotranspiration., 76, 5–16, 1963.
- Hinzman, L. D. and Kane, D. L.: Potential response of an Arctic watershed during a period of global warming, *J. Geophys.*
Res., 97, 2811, <https://doi.org/10.1029/91JD01752>, 1992.
- 765 Howie, S. A. and Hebda, R. J.: Bog surface oscillation (mire breathing): A useful measure in raised bog restoration,
Hydrological Processes, 32, 1518–1530, <https://doi.org/10.1002/hyp.11622>, 2018.
- Kämäräinen, A., Simojoki, A., Lindén, L., Jokinen, K., and Silvan, N.: Physical growing media characteristics of *Sphagnum*
770 biomass dominated by *Sphagnum fuscum* (Schimp.) Klinggr., 1–16, <https://doi.org/10.19189/MaP.2017.OMB.278>, 2018
- Khan, Z. A., Elkamel, A., and Gostick, J. T.: Efficient extraction of pore networks from massive tomograms via geometric
domain decomposition, *Advances in Water Resources*, 145, 103734, <https://doi.org/10.1016/j.advwatres.2020.103734>, 2020.
- Koponen, A., Kataja, M., and Timonen, J.: Tortuous flow in porous media, *Phys. Rev. E*, 54, 406–410,
775 <https://doi.org/10.1103/PhysRevE.54.406>, 1996.
- Koponen, A., Kataja, M., and Timonen, J.: Permeability and effective porosity of porous media, *Phys. Rev. E*, 56, 3319–
3325, <https://doi.org/10.1103/PhysRevE.56.3319>, 1997.

- 780 Launiainen, S., Katul, G. G., Lauren, A., and Kolari, P.: Coupling boreal forest CO₂, H₂O and energy flows by a vertically structured forest canopy – Soil model with separate bryophyte layer, *Ecological Modelling*, 312, 385–405, <https://doi.org/10.1016/j.ecolmodel.2015.06.007>, 2015.
- Leroy, P., Revil, A., Kemna, A., Cosenza, P., and Ghorbani, A.: Complex conductivity of water-saturated packs of glass
785 beads, *Journal of Colloid and Interface Science*, 321, 103–117, <https://doi.org/10.1016/j.jcis.2007.12.031>, 2008.
- Liljedahl, A. K., Boike, J., Daanen, R. P., Fedorov, A. N., Frost, G. V., Grosse, G., Hinzman, L. D., Iijma, Y., Jorgenson, J. C., Matveyeva, N., Necsoiu, M., Reynolds, M. K., Romanovsky, V. E., Schulla, J., Tape, K. D., Walker, D. A., Wilson, C. J., Yabuki, H., and Zona, D.: Pan-Arctic ice-wedge degradation in warming permafrost and its influence on tundra hydrology,
790 *Nature Geosci*, 9, 312–318, <https://doi.org/10.1038/ngeo2674>, 2016.
- Loranty, M. M., Abbott, B. W., Blok, D., Douglas, T. A., Epstein, H. E., Forbes, B. C., Jones, B. M., Kholodov, A. L., Kropp, H., Malhotra, A., Mamet, S. D., Myers-Smith, I. H., Natali, S. M., O'Donnell, J. A., Phoenix, G. K., Rocha, A. V., Sonnentag, O., Tape, K. D., and Walker, D. A.: Reviews and syntheses: Changing ecosystem influences on soil thermal
795 regimes in northern high-latitude permafrost regions, *Biogeosciences*, 15, 5287–5313, <https://doi.org/10.5194/bg-15-5287-2018>, 2018.
- Maalal, O., Prat, M., Peinador, R., and Lasseux, D.: Determination of the throat size distribution of a porous medium as an inverse optimization problem combining pore network modeling and genetic and hill climbing algorithms, *Phys. Rev. E*,
800 103, 023303, <https://doi.org/10.1103/PhysRevE.103.023303>, 2021.
- Malmström, C.: Some pointers for the drainage of peat soils in Noorland, 4, 1925.
- Martin, L. C. P., Nitzbon, J., Scheer, J., Aas, K. S., Eiken, T., Langer, M., Filhol, S., Etzelmüller, B., and Westermann, S.:
805 Lateral thermokarst patterns in permafrost peat plateaus in northern Norway, *The Cryosphere*, 15, 3423–3442, <https://doi.org/10.5194/tc-15-3423-2021>, 2021.
- McCarter, C. P. R. and Price, J. S.: Ecohydrology of *Sphagnum* moss hummocks: mechanisms of capitula water supply and simulated effects of evaporation: ECOHYDROLOGY OF *SPHAGNUM* MOSS HUMMOCKS, *Ecohydrol.*, 7, 33–44,
810 <https://doi.org/10.1002/eco.1313>, 2012
- McCarter, C. P. R., Rezanezhad, F., Quinton, W. L., Gharedaghloo, B., Lennartz, B., Price, J., Connon, R., and Van Cappellen, P.: Pore-scale controls on hydrological and geochemical processes in peat: Implications on interacting processes, *Earth-Science Reviews*, 207, 103227, <https://doi.org/10.1016/j.earscirev.2020.103227>, 2020.

- Meredith, M., Sommerkorn, M., Cassotta, S., Derksen, C., Ekaykin, A., Hollowed, A., Kofinas, G., Mackintosh, A., Melbourne-Thomas, J., . Muelbert, M. M. C., Ottersen, G., Pritchard, H., and Schuur, E. A. G.: IPCC Special Report on the Ocean and Cryosphere in a Changing Climate, 2019.
- 820 Mohammadmoradi, P. and Kantzas, A.: Pore-scale permeability calculation using CFD and DSMC techniques, *Journal of Petroleum Science and Engineering*, 146, 515–525, <https://doi.org/10.1016/j.petrol.2016.07.010>, 2016.
- O'Connor, M. T., Cardenas, M. B., Ferencz, S. B., Wu, Y., Neilson, B. T., Chen, J., and Kling, G. W.: Empirical Models for Predicting Water and Heat Flow Properties of Permafrost Soils, *Geophys. Res. Lett.*, 47,
825 <https://doi.org/10.1029/2020GL087646>, 2020.
- Olefeldt, D. and Roulet, N. T.: Permafrost conditions in peatlands regulate magnitude, timing, and chemical composition of catchment dissolved organic carbon export, *Glob Change Biol*, 20, 3122–3136, <https://doi.org/10.1111/gcb.12607>, 2014.
- Orgogozo, L., Prokushkin, A. S., Pokrovsky, O. S., Grenier, C., Quintard, M., Viers, J., and Audry, S.: Water and energy
830 transfer modeling in a permafrost-dominated, forested catchment of Central Siberia: The key role of rooting depth, *Permafrost and Periglac Process*, 30, 75–89, <https://doi.org/10.1002/ppp.1995>, 2019.
- Otsu, N.: A Threshold Selection Method from Gray-Level Histograms, *IEEE Trans. Syst., Man, Cybern.*, 9, 62–66,
835 <https://doi.org/10.1109/TSMC.1979.4310076>, 1979.
- Päivänen, J.: Hydraulic conductivity and water retention in peat soils, *Acta For. Fenn.*, 0, <https://doi.org/10.14214/aff.7563>, 1973.
- Park, H., Launiainen, S., Konstantinov, P. Y., Iijima, Y., and Fedorov, A. N.: Modeling the Effect of Moss Cover on Soil
840 Temperature and Carbon Fluxes at a Tundra Site in Northeastern Siberia, *J. Geophys. Res. Biogeosci.*, 123, 3028–3044, <https://doi.org/10.1029/2018JG004491>, 2018.
- Patankar, S. V.: Numerical heat transfer and fluid flow, Hemisphere Publ. Co, New York, 197 pp., 1980.
- 845 Payandi-Rolland, D., Shirokova, L. S., Tesfa, M., Bénézech, P., Lim, A. G., Kuzmina, D., Karlsson, J., Giesler, R., and Pokrovsky, O. S.: Dissolved organic matter biodegradation along a hydrological continuum in permafrost peatlands, *Science of The Total Environment*, 749, 141463, <https://doi.org/10.1016/j.scitotenv.2020.141463>, 2020.
- Porada, P., Ekici, A., and Beer, C.: Effects of bryophyte and lichen cover on permafrost soil temperature at large scale, *The
850 Cryosphere*, 10, 2291–2315, <https://doi.org/10.5194/tc-10-2291-2016>, 2016.

Potkay, A., ten Veldhuis, M., Fan, Y., Mattos, C. R. C., Ananyev, G., and Dismukes, G. C.: Water and vapor transport in algal-fungal lichen: Modeling constrained by laboratory experiments, an application for *Flavoparmelia caperata*, *Plant Cell Environ*, 43, 945–964, <https://doi.org/10.1111/pce.13690>, 2020.

855

Price, J. S. and Whittington, P. N.: Water flow in Sphagnum hummocks: Mesocosm measurements and modelling, *Journal of Hydrology*, 381, 333–340, <https://doi.org/10.1016/j.jhydrol.2009.12.006>, 2010.

860 Price, J. S., Whittington, P. N., Elrick, D. E., Strack, M., Brunet, N., and Faux, E.: A Method to Determine Unsaturated Hydraulic Conductivity in Living and Undecomposed *Sphagnum* Moss, *Soil Sci. Soc. Am. J.*, 72, 487–491, <https://doi.org/10.2136/sssaj2007.0111N>, 2008.

Puustjärvi, V.: Peat and its use in horticulture, *Turveteollisuusliitto*, Helsinki, 160 pp., 1977.

865

Quintard, M. and Whitaker, S.: Ecoulement monophasique en milieux poreux : effet des hétérogénéités, 691–726, 1989.

Quinton, W. L., Gray, D. M., and Marsh, P.: Subsurface drainage from hummock-covered hillslopes in the Arctic tundra, *Journal of Hydrology*, 237, 113–125, [https://doi.org/10.1016/S0022-1694\(00\)00304-8](https://doi.org/10.1016/S0022-1694(00)00304-8), 2000.

870 Raudina, T. V., Loiko, S. V., Lim, A., Manasypov, R. M., Shirokova, L. S., Istigechev, G. I., Kuzmina, D. M., Kulizhsky, S. P., Vorobyev, S. N., and Pokrovsky, O. S.: Permafrost thaw and climate warming may decrease the CO₂, carbon, and metal concentration in peat soil waters of the Western Siberia Lowland, *Science of The Total Environment*, 634, 1004–1023, <https://doi.org/10.1016/j.scitotenv.2018.04.059>, 2018.

875 Rezanezhad, F., Price, J. S., Quinton, W. L., Lennartz, B., Milojevic, T., and Van Cappellen, P.: Structure of peat soils and implications for water storage, flow and solute transport: A review update for geochemists, *Chemical Geology*, 429, 75–84, <https://doi.org/10.1016/j.chemgeo.2016.03.010>, 2016.

880 Roux, N., Costard, F., and Grenier, C.: Laboratory and Numerical Simulation of the Evolution of a River’s Talik: Laboratory and Numerical Simulations of river’s Talik Evolution, *Permafrost and Periglac. Process.*, 28, 460–469, <https://doi.org/10.1002/ppp.1929>, 2017.

Sadeghi, A. and Gostick, J.: Berea Sandstone Simulation Using PoreSpy and OpenPNM, PMEAL, University of Waterloo, ON, Canada, 2020.

885

Sarasto, J.: Tutkimuksia rahka- ja saraturpeiden vedenläpäisevyydestä | A study of the permeability to water of different kind of peat, 32–36, 1963.

- Schindelin, J., Arganda-Carreras, I., Frise, E., Kaynig, V., Longair, M., Pietzsch, T., Preibisch, S., Rueden, C., Saalfeld, S., Schmid, B., Tinevez, J.-Y., White, D. J., Hartenstein, V., Eliceiri, K., Tomancak, P., and Cardona, A.: Fiji: an open-source platform for biological-image analysis, *Nat Methods*, 9, 676–682, <https://doi.org/10.1038/nmeth.2019>, 2012.
- Shi, X., Ricciuto, D. M., Thornton, P. E., Xu, X., Yuan, F., Norby, R. J., Walker, A. P., Warren, J. M., Mao, J., Hanson, P. J., Meng, L., Weston, D., and Griffiths, N. A.: Extending a land-surface model with *Sphagnum* moss to simulate responses of a northern temperate bog to whole ecosystem warming and elevated CO₂. *Biogeosciences*, 18, 467–486, <https://doi.org/10.5194/bg-18-467-2021>, 2021.
- Shirokova, L. S., Chupakov, A. V., Ivanova, I. S., Moreva, O. Y., Zabelina, S. A., Shutskiy, N. A., Loiko, S. V., and Pokrovsky, O. S.: Lichen, moss and peat control of C, nutrient and trace metal regime in lakes of permafrost peatlands, *Science of The Total Environment*, 146737, <https://doi.org/10.1016/j.scitotenv.2021.146737>, 2021.
- Silin, D. and Patzek, T.: Pore space morphology analysis using maximal inscribed spheres, *Physica A: Statistical Mechanics and its Applications*, 371, 336–360, <https://doi.org/10.1016/j.physa.2006.04.048>, 2006.
- Soudzilovskaia, N. A., van Bodegom, P. M., and Cornelissen, J. H. C.: Dominant bryophyte control over high-latitude soil temperature fluctuations predicted by heat transfer traits, field moisture regime and laws of thermal insulation, *Funct Ecol*, 27, 1442–1454, <https://doi.org/10.1111/1365-2435.12127>, 2013.
- Soulaine, C., Gjetvåg, F., Garing, C., Roman, S., Russian, A., Gouze, P., and Tchelepi, H. A.: The Impact of Sub-Resolution Porosity of X-ray Microtomography Images on the Permeability, *Transp Porous Med*, 113, 227–243, <https://doi.org/10.1007/s11242-016-0690-2>, 2016.
- Stepanenko, V. M., Repina, I. A., Fedosov, V. E., Zilitinkevich, S. S., and Lykossov, V. N.: An Overview of Parameterizations of Heat Transfer over Moss-Covered Surfaces in the Earth System Models, *Izv. Atmos. Ocean. Phys.*, 56, 101–111, <https://doi.org/10.1134/S0001433820020139>, 2020.
- Strack, M., Waddington, J. M., Lucchese, M. C., and Cagampan, J. P.: Moisture controls on CO₂ exchange in a *Sphagnum* - dominated peatland: results from an extreme drought field experiment, *Ecohydrol.*, 2, 454–461, <https://doi.org/10.1002/eco.68>, 2009.
- Streletskiy, D. A., Tananaev, N. I., Opel, T., Shiklomanov, N. I., Nyland, K. E., Streletskaya, I. D., Tokarev, I., and Shiklomanov, A. I.: Permafrost hydrology in changing climatic conditions: seasonal variability of stable isotope composition in rivers in discontinuous permafrost, *Environ. Res. Lett.*, 10, 095003, <https://doi.org/10.1088/1748-9326/10/9/095003>, 2015.
- Tananaev, N., Teisserenc, R., and Debolskiy, M.: Permafrost Hydrology Research Domain: Process-Based Adjustment, *Hydrology*, 7, 6, <https://doi.org/10.3390/hydrology7010006>, 2020.

- Tarhanen, S., Metsärinne, S., Holopainen, T., and Oksanen, J.: Membrane permeability response of lichen *Bryoria fuscescens* to wet deposited heavy metals and acid rain, *Environmental Pollution*, 104, 121–129, [https://doi.org/10.1016/S0269-7491\(98\)00157-2](https://doi.org/10.1016/S0269-7491(98)00157-2), 1999.
- 930 Throckmorton, H. M., Newman, B. D., Heikoop, J. M., Perkins, G. B., Feng, X., Graham, D. E., O'Malley, D., Vesselinov, V. V., Young, J., Wulfschleger, S. D., and Wilson, C. J.: Active layer hydrology in an arctic tundra ecosystem: quantifying water sources and cycling using water stable isotopes: Active Layer Hydrology in the Arctic Coastal Plain, *Hydrol. Process.*, 30, 4972–4986, <https://doi.org/10.1002/hyp.10883>, 2016.
- 935 Turberg, P., Zeimet, F., Grondin, Y., Elandoy, C., and Buttler, A.: Characterization of structural disturbances in peats by X-ray CT-based density determinations: Characterization of structural disturbances in peats, *Eur J Soil Sci*, 65, 613–624, <https://doi.org/10.1111/ejss.12148>, 2014.
- 940 Védie, E., Lagarde, J.-L., and Font, M.: Physical modelling of rainfall- and snowmelt-induced erosion of stony slope underlain by permafrost, *Earth Surf. Process. Landforms*, 36, 395–407, <https://doi.org/10.1002/esp.2054>, 2011.
- Virta, J.: Suohydrologisista tutkimuksista Lapissa ja Pohjanmaalla | On the research of peat land hydrology in Lapland and Ostrobothnia, 30–35, 1962.
- 945 Volkova, I. I., Kolesnichenko, L. G., Volkova, A. I., Obuchova, A. Y., Pokrovsky, O. S., and Vorobyev, S. N.: Peat Forming Mosses as a Key Component of Peat Deposits and Mire Vegetation of the West Siberian Taiga, in: *Mosses: ecology, life cycle and significance*, edited by: Pokrovsky, O. S., Volkova, I., Kosykh, N., and Shevchenko, V., Nova Science Publishers, Incorporated, New York, 175–189, 2018.
- 950 Voortman, B. R., Bartholomeus, R. P., van Bodegom, P. M., Gooren, H., van der Zee, S. E. A. T. M., and Witte, J.-P. M.: Unsaturated hydraulic properties of xerophilous mosses: towards implementation of moss covered soils in hydrological models: UNSATURATED HYDRAULIC PROPERTIES OF XEROPHILOUS MOSSES, *Hydrol. Process.*, 28, 6251–6264, <https://doi.org/10.1002/hyp.10111>, 2014.
- 955 Wagner, A. M., Lindsey, N. J., Dou, S., Gelvin, A., Saari, S., Williams, C., Ekblaw, I., Ulrich, C., Borglin, S., Morales, A., and Ajo-Franklin, J.: Permafrost Degradation and Subsidence Observations during a Controlled Warming Experiment, *Sci Rep*, 8, 10908, <https://doi.org/10.1038/s41598-018-29292-y>, 2018.
- Walvoord, M. A. and Kurylyk, B. L.: Hydrologic Impacts of Thawing Permafrost-A Review, *Vadose Zone Journal*, 15, 960 vj2016.01.0010, <https://doi.org/10.2136/vzj2016.01.0010>, 2016.

Weber, T. K. D., Iden, S. C., and Durner, W.: Unsaturated hydraulic properties of *Sphagnum* moss and peat reveal trimodal pore-size distributions: TRIMODAL HYDRAULIC PROPERTIES OF *SPHAGNUM* MOSS, *Water Resour. Res.*, 53, 415–434, <https://doi.org/10.1002/2016WR019707>, 2017.

965

Weller, H. G., Tabor, G., Jasak, H., and Fureby, C.: A tensorial approach to computational continuum mechanics using object-oriented techniques, 12, 620–631, 1998.

Whitaker, S.: *The Method of Volume Averaging*, Springer, Dordrecht, 1999.

970 Yi, S., Manies, K., Harden, J., and McGuire, A. D.: Characteristics of organic soil in black spruce forests: Implications for the application of land surface and ecosystem models in cold regions, *Geophys. Res. Lett.*, 36, L05501, <https://doi.org/10.1029/2008GL037014>, 2009.

Zhang, D., Zhang, R., Chen, S., and Soll, W. E.: Pore scale study of flow in porous media: Scale dependency, REV, and
975 statistical REV, *Geophys. Res. Lett.*, 27, 1195–1198, <https://doi.org/10.1029/1999GL011101>, 2000.

Declarations

Funding: French Research Agency (ANR) - HiPerBorea project (ANR-19 CE46-0003-01) / CNRS (BryoPhyGel project) / French embassy in Russia (PHC Kolmogorov project 2017 N° 38144TB) / Russian Science Foundation (project no. 18-77-10045).
980

Conflict of interest: All authors certify that they have no affiliations with or involvement in any organization or entity with any financial interest or non-financial interest in the subject matter or materials discussed in this manuscript.

Availability of data and material: Material is available on the project’s website (www.hiperborea.omp.eu).

985 **Author contributions:**

Funding acquisition & Project administration: Laurent Orgogozo.

Conceptualization, Supervision & Validation: Manuel Marcoux, Laurent Orgogozo.

Investigation, Formal analysis, software, Data curation, visualization & Writing original draft: Simon Cazaurang.

Resources, Field Methodology: Serguey Loiko, Artem Lim, Stéphane Audry, Liudmila Shirokova, Oleg Pokrovsky,
990 Georgiy Istigechev.

Reviewing: Manuel Marcoux, Laurent Orgogozo, Serguey Loiko, Artem Lim, Stéphane Audry, Liudmila Shirokova, Oleg Pokrovsky.

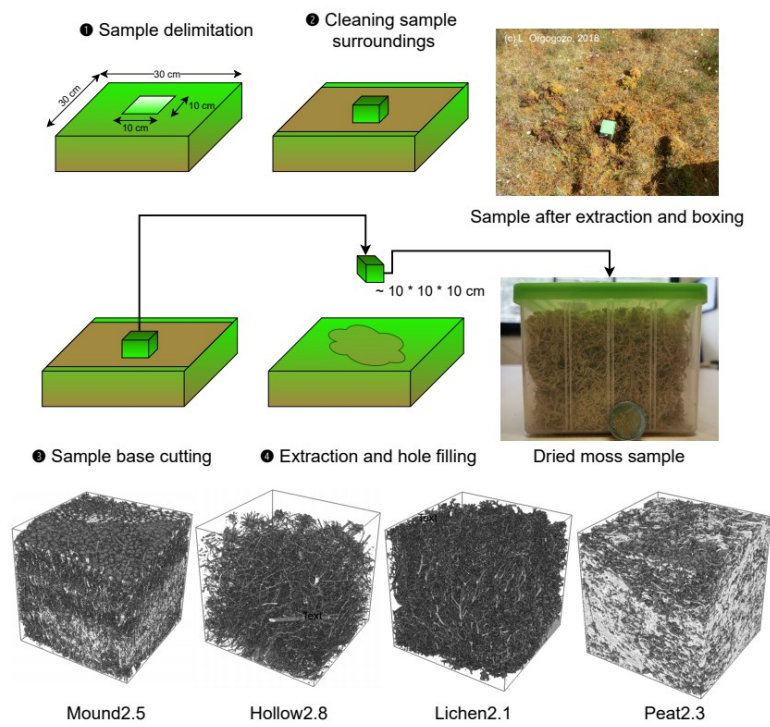


Figure 1: Sampling collection method overview.

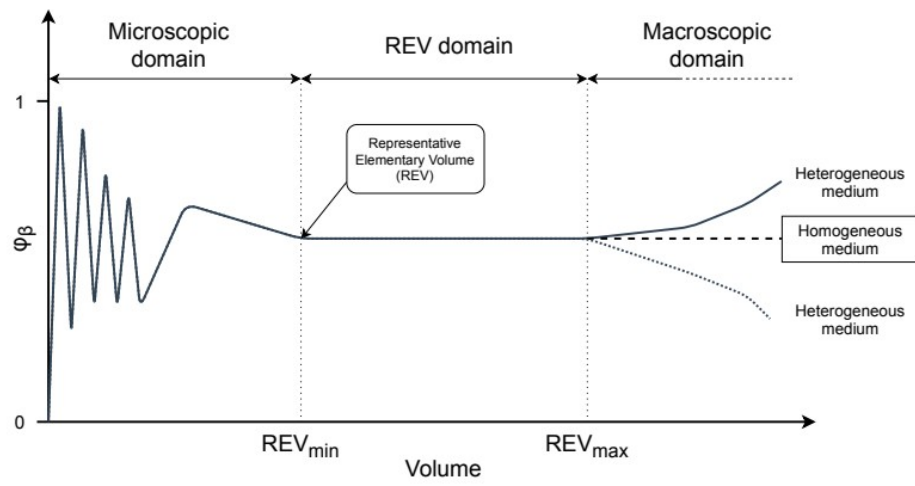
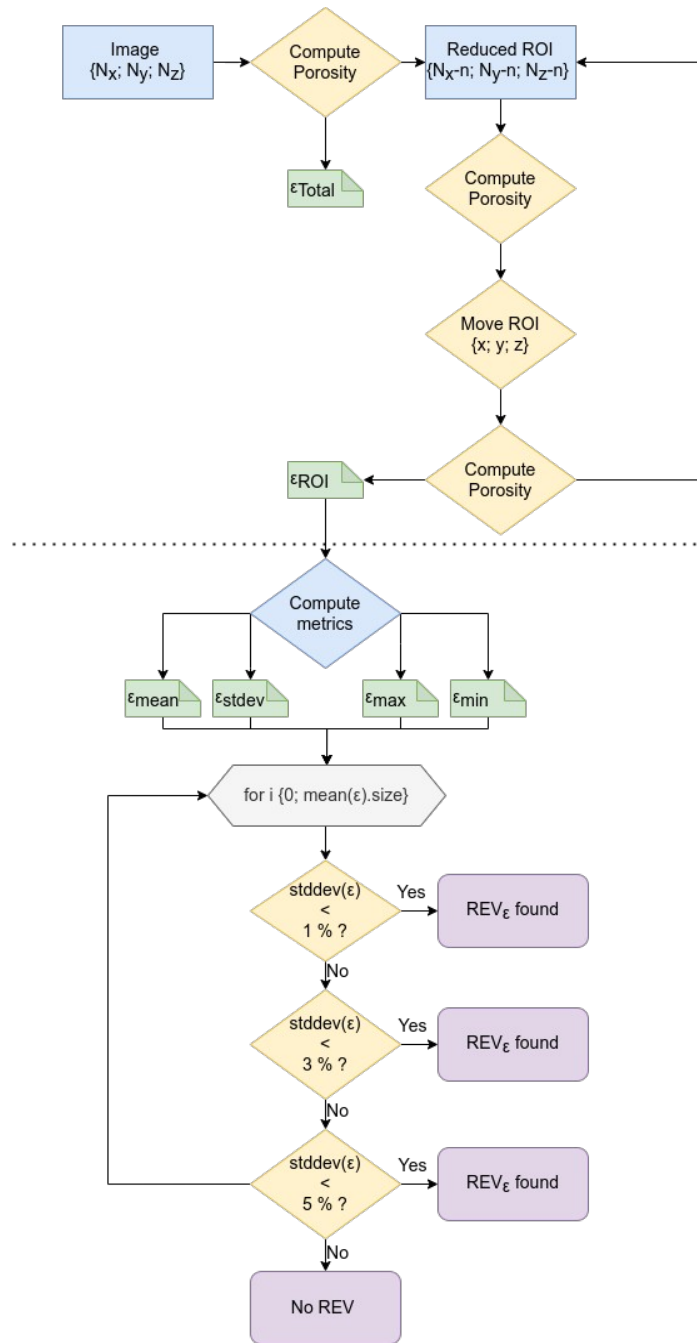


Figure 2: Schematic representation of fluctuations of a generic property ϕ_β in conjunction with volume (adapted after Brown & Hsieh, 2000).



1005 **Figure 3: Flowchart of Representative Elementary Volume of Porosity (REV_ϵ) from binarized image. For each sample, three thresholds are tested (5 %, 3% and 1 % and standard deviation variation).**

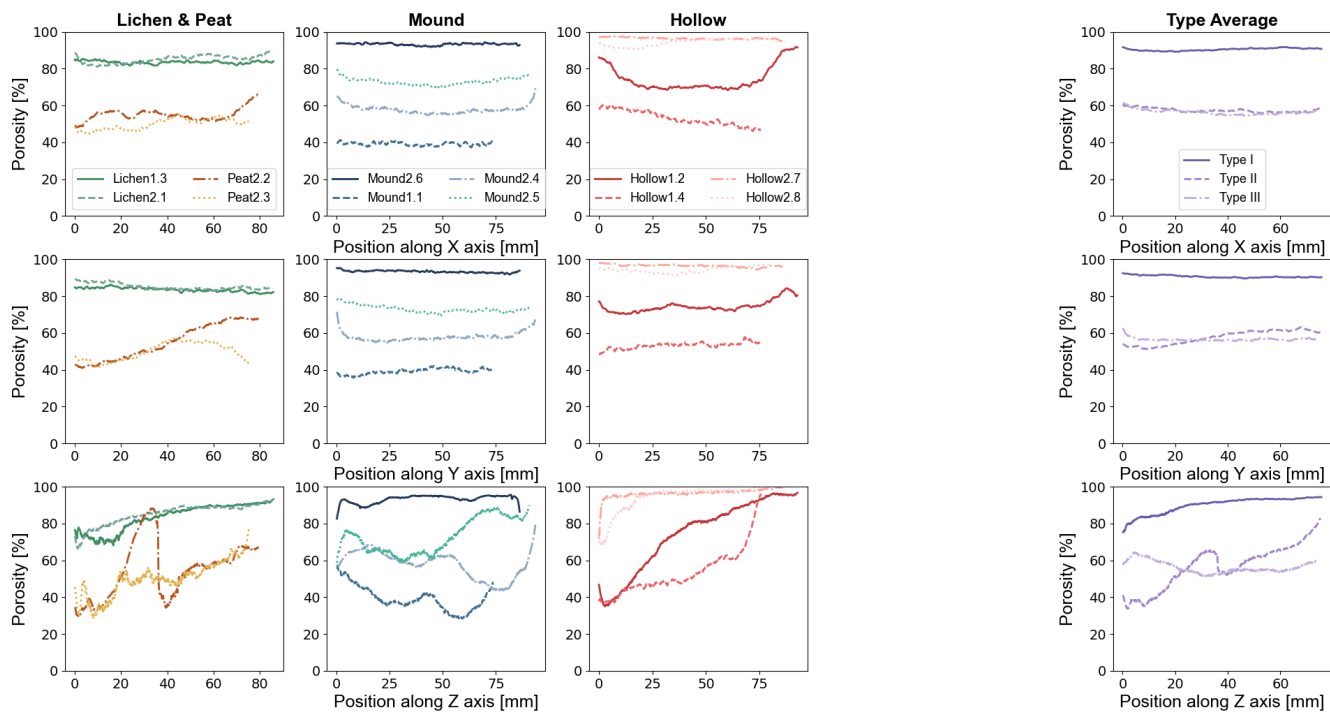
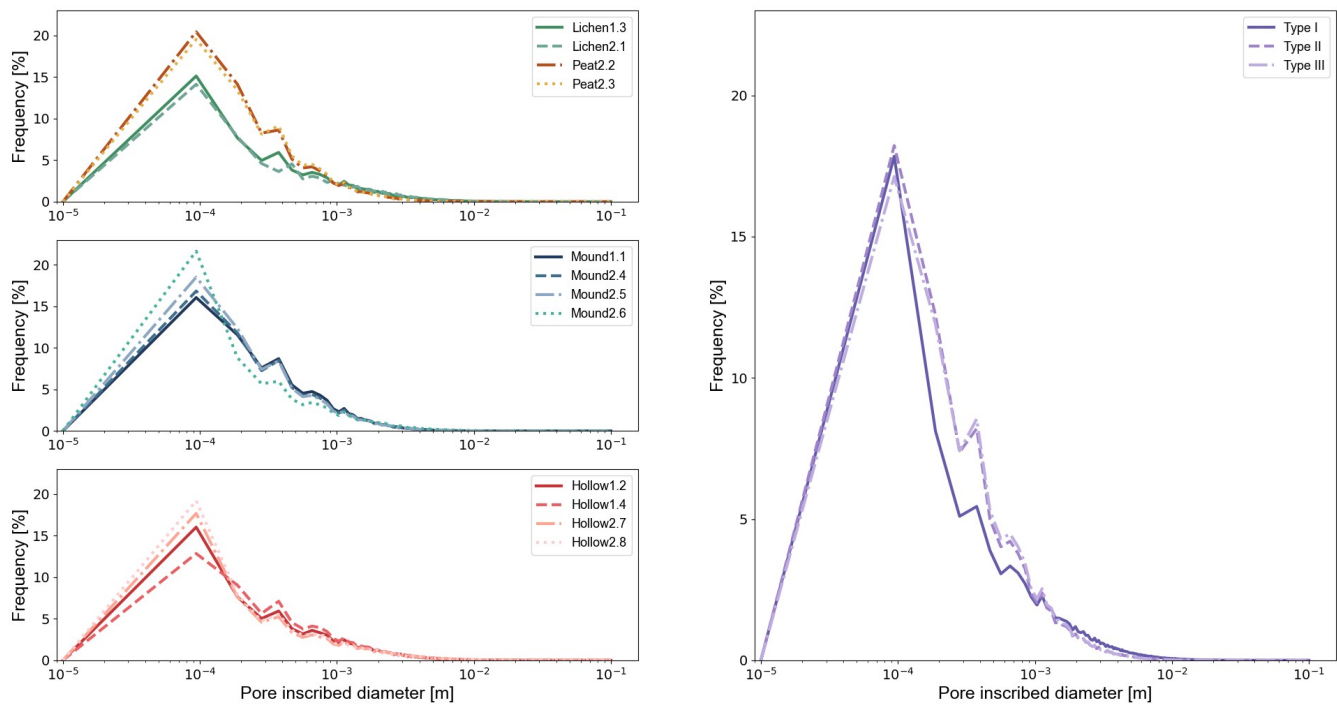


Figure 4: Planar porosity plot along x , y , and z axis for moss, lichen and peat samples. An averaged value is computed for each sample type, each color nuance representing each type. *Type I: Stable high porosity profile samples, excluding border effects; Type II: Low basal porosity, linearly increasing to the top of the sample; Type III: No specific trend observed on vertical porosity.*



1015 **Figure 5: Incribed pore size distribution by classified type using particles' Feret diameter measurement. An averaged value is computed for each sample type, each colour nuance representing each type.**

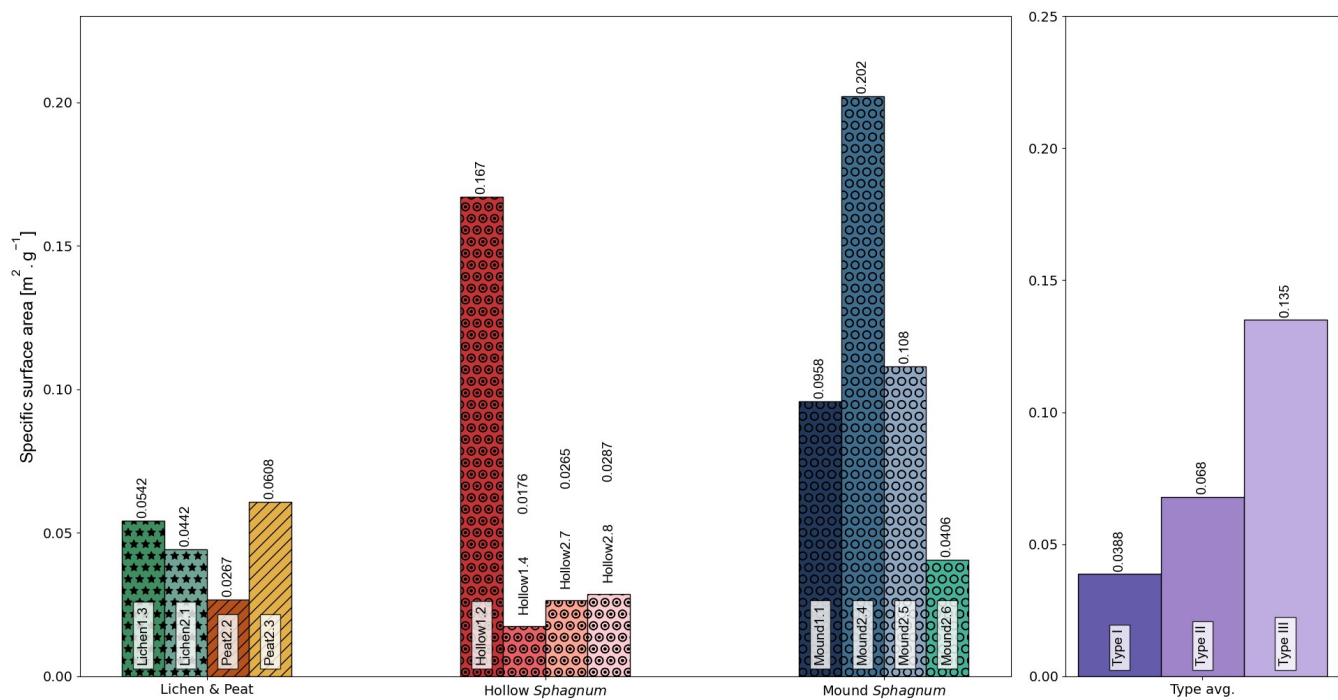


Figure 6: Specific surface area [in $\text{m}^2 \cdot \text{g}^{-1}$] plots for each sample. Colors refer to each sample type.

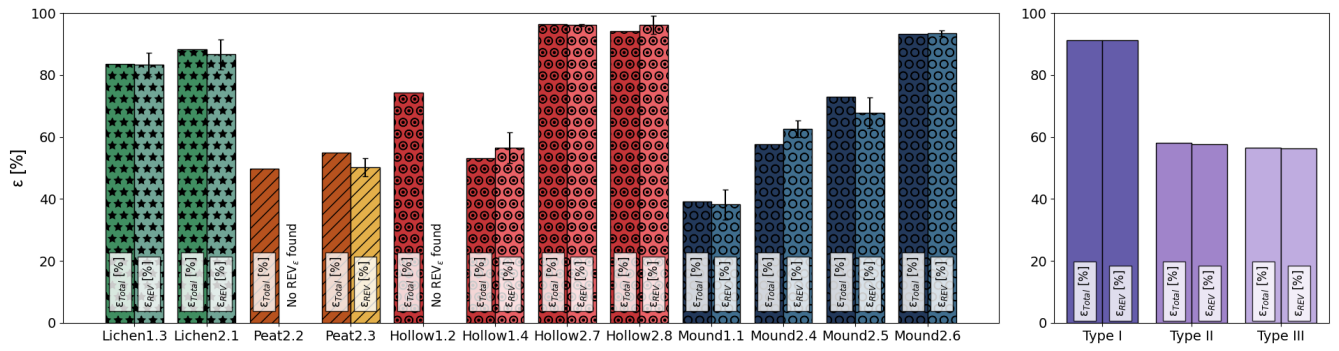


Figure 7: Numerical porosity estimations [in %] for each sample. An averaged value is computed for each identified sample type (I, II, III) with corresponding color nuances. Peat 2.2 and Hollow1.2 did not admit any REV.

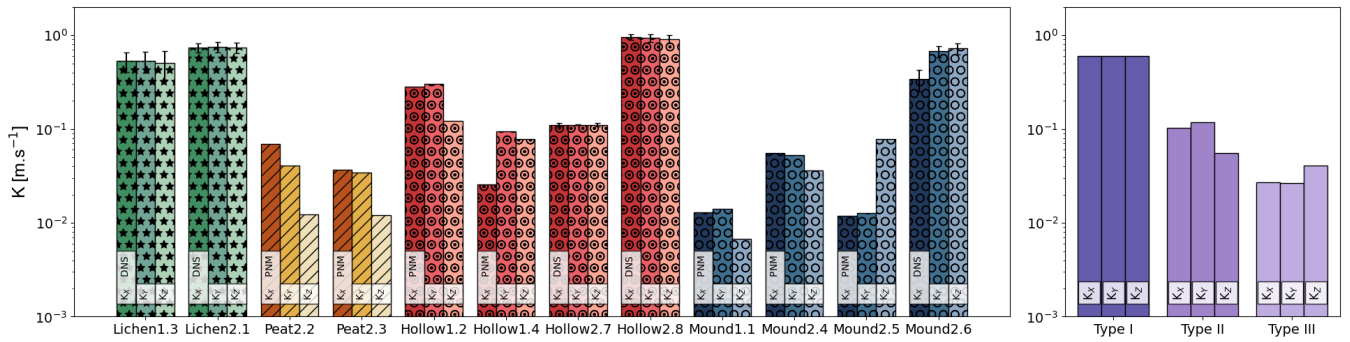
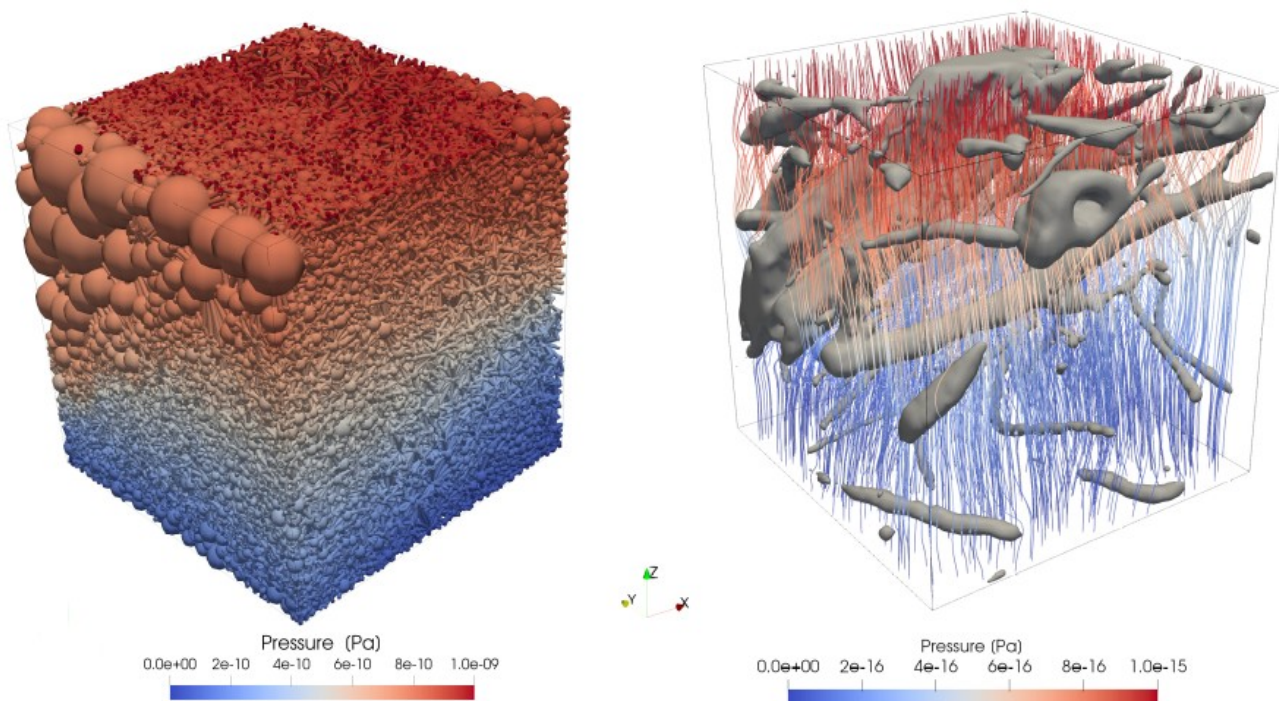


Figure 8: Diagonal components of the hydraulic conductivity tensor (in m.s^{-1}) in x (K_{xx}), y (K_{yy}) and z axis (K_{zz}) based on Direct Numerical Simulations (DNS) on Representative Elementary Volume of hydraulic conductivity (REV_K) for Type I samples and with a Pore Network Model (PNM) for Type II and III samples.



1035 **Figure 9: (Left)** Pressure field (in Pa) after a single-phase flow simulation thorough a pore network model based on Mound2.5 sample. Spherical pore sizes are represented according to their respective size in the network. **(Right)** Pressure field lines (in Pa) after a single-phase flow simulation through a sub-sample of Hollow2.8 sample. The gray mesh corresponds to the isolated biological phase.

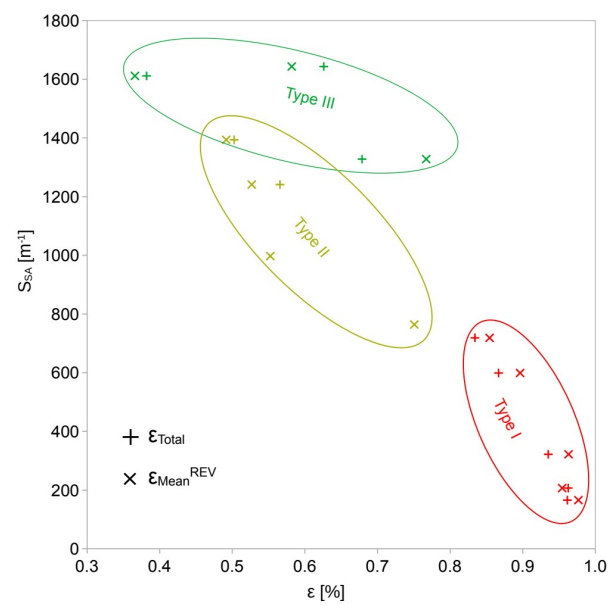


Figure 10: Specific Surface (in m^{-1}) as a function of total porosity ϵ_{Total} [%] and Representative Elementary averaged porosity ϵ_{mean}^{REV} [%].

Table 1: Notation Glossary.

Symbol	Description	Unit
Greek letters		
ρ_{dry}	Dried bulk sample density	$\text{kg} \cdot \text{m}^{-3}$
ρ_w	Water density	$\text{kg} \cdot \text{m}^{-3}$
ϵ_{total}	Sample digital overall porosity	%
ϵ_{open}	Sample digital open porosity	%
μ_w	Dynamic viscosity of water	$\text{Pa} \cdot \text{s}^{-1}$
σ	Generic symbol for ratios	—
$\sigma_{\text{S-T}}$	Ratio between sphere number and throat number (pore network)	—
Roman letters		
d_{Sph}	Spherical pore density (pore network)	m^{-3}
d_{Thr}	Throat density (pore network)	m^{-3}
g	Gravitational acceleration	$\text{m} \cdot \text{s}^{-2}$
i_{voxel}	Voxel intensity	—
k	Intrinsic permeability	m^2
K_w	Hydraulic conductivity	$\text{m} \cdot \text{s}^{-1}$
L_i	Sample length along axis i	m
L_e^{REV}	Representative Elementary Volume of porosity edge length	mm
L_K^{REV}	Representative Elementary Volume of hydraulic conductivity edge length	mm
N_b	Number of voxels of intensity $N = b$	—
p_{open}	Ratio between ϵ_{open} and ϵ_{total}	—
P	Pressure (water head)	Pa
Re	Reynolds number	—
S_{outlet}	Overall surface of the outlet (including void and solid phase)	m^2
$S_{\text{SA(M)}}$	Mass specific surface area	$\text{m}^2 \cdot \text{g}^{-1}$
$S_{\text{SA(V)}}$	Volumetric specific surface area	$\text{m}^2 \cdot \text{m}^{-3}$
V_v	Volume of an array v	m^3
v_i	Incompressible flow speed along direction i	$\text{m} \cdot \text{s}^{-1}$
u_i	Darcy flow along axis i	$\text{m}^3 \cdot \text{s}^{-1}$

Table 2: Synthesis of saturated hydraulic conductivity (in m.s⁻¹) of peat and *Sphagnum* found in the literature. *This study*’s values refer to field experiments conducted during sample collection (CHP: Constant Head Permeameter; FHP: Falling Head Permeameter; FP: Field Percolation; IM: Inverse Modelling; NM: Numerical Model (Hydrus-1D, see McCarter & Price, 2012)).

Sample	Method	K _w [m.s ⁻¹]	Reference
Lichen	IM	1.8·10 ⁻⁹ – 3.7·10 ⁻⁹	Voortmann et al., 2014
Peat	CHP	4.6·10 ⁻⁶ – 4.2·10 ⁻⁴	Hamamoto et al., 2016
Peat	CHP	3·10 ⁻⁵ – 1.3·10 ⁻³	Quinton et al., 2000
<i>Sphagnum</i>	CHP	1.1·10 ⁻² – 4.3·10 ⁻²	Golubev et al., 2021
<i>Sphagnum</i>	Modified CHP	2.4·10 ⁻⁴ – 1.8·10 ⁻³	Price et al., 2008
<i>Sphagnum</i>	FHP	1.2·10 ⁻⁴ – 1.2·10 ⁻³	Weber et al., 2017
Peat	FP	1.7·10 ⁻⁶ – 3.3·10 ⁻⁵	Päivänen, 1973
<i>Sphagnum</i>	FP	5.6·10 ⁻⁵ – 1.7·10 ⁻⁴	Crockett et al., 2016
<i>Sphagnum</i>	NM	2.9·10 ⁻⁵ – 3.2·10 ⁻³	McCarter & Price, 2012
<i>Sphagnum</i>	FP	6·10 ⁻⁵ – 2·10 ⁻⁴	This study

Table 3: Computed global porosity (ε_{total}), ratio of open porosity (p_{open}), classification (I, II, III) and average planar porosity [%] for each sample obtained using a voxel counting algorithm.

Sample	ε _{total} [%]	p _{open} [-]	Class	ε _{X(Class)} [%]	ε _{Y(Class)} [%]	ε _{Z(Class)} [%]
Lichen1.3	83.5	0.9999	I	90.6 ± 0.7	90.6 ± 0.6	90.0 ± 4.4
Lichen2.1	88.2	0.9999				
Mound2.6	93.3	0.9999				
Hollow2.7	96.5	0.9999				
Hollow2.8	94.3	0.9999	II	57.4 ± 1.2	57.5 ± 3.7	56.7 ± 11.8
Hollow1.2	74.4	0.9984				
Hollow1.4	53.1	0.9980				
Peat2.2	49.8	0.9931				
Peat2.3	55.0	0.9938	III	56.7 ± 1.3	56.5 ± 0.8	56.2 ± 3.2
Mound1.1	39.1	0.9917				
Mound2.4	57.7	0.9900				
Mound2.5	72.9	0.9998				

Table 4: Obtained Representative Elementary Volume based on porosity (REV_ϵ). L_ϵ^{REV} is the side length of a cubic REV of porosity. ϵ_{mean}^{REV} is the average porosity of a given cubic REV. Ratio represents the volumetric percentage of the sample included in the REV.

Sample	L_ϵ^{REV} [mm]	ϵ_{mean}^{REV} [%]	Ratio [%]
Hollow1.2	No REV	74.4	100
Hollow1.4	13.4	56.6 (± 4.9)	17.4
Hollow2.7	2.82	96.1 (± 0.3)	3.3
Hollow2.8	7.52	96.3 (± 3.0)	9.4
Lichen1.3	1.88	83.4 (± 3.9)	2.1
Lichen2.1	14.1	86.7 (± 4.9)	16.5
Mound1.1	5.64	38.2 (± 4.9)	7.7
Mound2.4	9.40	62.6 (± 2.7)	10.0
Mound2.5	11.3	67.9 (± 4.9)	12.4
Mound2.6	26.3	93.5 (± 1.0)	30.5
Peat2.2	No REV	49.8	100
Peat2.3	3.76	50.3 (± 3.0)	5.1

1060

Table 5: Diagonal components of the hydraulic conductivity tensor (in $m.s^{-1}$) for the studied Representative Elementary Volumes of hydraulic conductivity (REV_K) for type I samples using Direct Numerical Simulations.

Sample	L_K^{REV} [mm]	K_{xx}^{REV} [$m.s^{-1}$]	K_{yy}^{REV} [$m.s^{-1}$]	K_{zz}^{REV} [$m.s^{-1}$]
Hollow2.7	15.7 (167 vx)	$1.1 \cdot 10^{-1} (\pm 5.0 \cdot 10^{-3})$	$1.1 \cdot 10^{-1} (\pm 6.07 \cdot 10^{-4})$	$1.1 \cdot 10^{-1} (\pm 5.1 \cdot 10^{-3})$
Hollow2.8	15.7 (167 vx)	$9.5 \cdot 10^{-1} (\pm 6.6 \cdot 10^{-2})$	$9.3 \cdot 10^{-1} (\pm 8.73 \cdot 10^{-2})$	$9.1 \cdot 10^{-1} (\pm 9.4 \cdot 10^{-2})$
Lichen1.3	9.4 (100 vx)	$5.3 \cdot 10^{-1} (\pm 1.3 \cdot 10^{-1})$	$5.3 \cdot 10^{-1} (\pm 1.31 \cdot 10^{-1})$	$5.1 \cdot 10^{-1} (\pm 1.7 \cdot 10^{-1})$
Lichen2.1	15.7 (167 vx)	$7.4 \cdot 10^{-1} (\pm 8.3 \cdot 10^{-2})$	$7.5 \cdot 10^{-1} (\pm 9.46 \cdot 10^{-2})$	$7.4 \cdot 10^{-1} (\pm 9.6 \cdot 10^{-2})$
Mound2.6	11.8 (125 vx)	$6.8 \cdot 10^{-1} (\pm 9.0 \cdot 10^{-2})$	$6.7 \cdot 10^{-1} (\pm 9.1 \cdot 10^{-2})$	$7.2 \cdot 10^{-1} (\pm 9.9 \cdot 10^{-2})$

1065 **Table 6: Hydraulic conductivity values (in m.s⁻¹) obtained using a double-ring infiltrometer during sampling campaign.**

Sample	Date	K _{field} [m.s ⁻¹]
Hollow1.2	26.07.2018	1.8·10 ⁻⁴
Hollow2.7	27.07.2018	9.3·10 ⁻⁵
Hollow2.8	27.07.2018	5.6·10 ⁻⁵
Lichen2.1	27.07.2018	9.9·10 ⁻⁴
Mound1.1	26.07.2018	1.8·10 ⁻⁴
Mound2.4	27.07.2018	> 10 ⁻⁴
Mound2.6	27.07.2018	> 10 ⁻⁴